OBSERVATIONS AÉRIENNES DE LA FRAGMENTATION DE LA BANQUISE PAR DES VAGUES DE NAVIRE

MÉMOIRE PRÉSENTÉ

dans le cadre du programme de maîtrise en océanographie

en vue de l'obtention du grade de maître ès sciences

PAR

©ELIE DUMAS-LEFEBVRE

Avril 2021

Composition du jury :

Bruno Tremblay, examinateur externe, Université McGill

Dany Dumont, directeur de recherche, Université du Québec à Rimouski

Daniel Bourgault, codirecteur de recherche, Université du Québec à Rimouski

Cédric Chavanne, président du jury, Université du Québec à Rimouski

Dépôt initial le 17 décembre 2020 Dépôt final le 8 avril 2021

REMERCIEMENTS

Tout d'abord j'aimerais remercier prof. Dany Dumont, mon directeur de maîtrise, pour toutes les opportunités qu'il m'a apporté et pour la liberté qu'il m'a laissé tout au long de ce parcours. Merci pour ta confiance Dany, ça m'a permis d'en développer une envers moi-même. J'aimerais aussi remercier Jérémy Baudry pour l'aide qu'il m'a fourni et les réflexions qu'il m'a amené tout au long de ma maîtrise. Un gros merci à James Caveen [1] pour toute l'aide au niveau informatique. Merci à prof. Daniel Bourgault, co-directeur de cette maîtrise, pour son dynamisme, ses commentaires et la correction de mon mémoire. Merci à Félix Lamarche pour l'inspiration artisique liée à la glace. Merci à mes amis qui m'ont permis de prendre un pas de recul sur ma maîtrise et qui m'ont fait tant apprendre au cours des deux dernières années. Merci Jade, celle avec qui je partage ma vie et mes nouvelles idées de façon parfois peu vulgarisée, pour ton soutien et tes encouragements tout au long des dernières années.

Je tiens à remercier les Fonds de recherche du Québec Nature et technologie (FRQNT), le Conseil de recherches en cciences naturelles et en génie du Canada (CRSNG), l'Institut des sciences de la mer de Rimouski (ISMER) et prof. Dany Dumont pour le soutien financier pendant ma maîtrise. Merci au Réseau Québec maritime (RQM) de m'avoir permis de participer à la deuxième édition hivernale de la mission Odyssée Saint-Laurent (OSL) sans laquelle mon projet de maîtrise ne serait pas ce qu'il est aujourd'hui. Merci à ArcticNet et à Jean Carlos Montero Serrano pour l'opportunité d'effectuer une deuxième expérience de fragmentation dans l'Arctique canadien.

---

1. Certains soupçonnent qu'il soit lui-même la grappe de calcul.

RÉSUMÉ

La zone marginale de glace (MIZ) est une région de la banquise caractérisée par la variabilité de la taille des morceaux de glace (floes) qui la composent et par son interaction avec les vagues. Qu'ils soient de nature mécanique ou thermodynamique, la majorité des processus qui se produisent dans cette étendue sont dépendant de la taille des floes. Les observations disponibles actuellement rendent un portrait global de la distribution spatiale de la taille des floes (FSD) qui ne permet pas de comprendre l'influence de chacun des processus sur sa forme. Les objectifs principaux de cette maîtrise sont d'observer l'influence de la fragmentation de la glace par les vagues sur la FSD et d'analyser l'évolution temporelle de ce phénomène. Ces observations serviront à approfondir les connaissances fondamentales de la dynamique de la MIZ et à améliorer la représentation de la taille des floes dans les modèles. On croit que ce processus génère une taille préférentielle mais il est à savoir si celle-ci est contrainte par la rigidité flexurale de la glace ou plutôt par la longueur d'onde de la vague principale causant les déflections. Pour vérifier cette hypothèse, deux expériences ont été effectuées : une dans le golfe du Saint-Laurent à l'hiver 2019 et l'autre dans la baie de Baffin à l'été 2019, au cours desquelles des vagues ont été générées par le *NGCC* Amundsen afin de casser la glace. Le tout a été filmé et photographié par un drone afin de pouvoir en extraire la FSD et l'évolution temporelle. Lorsque représentée sous la forme d'une densité de probabilité, la FSD exhibe une forme modale et confirme donc l'hypothèse de la taille préférentielle. Une distance de fracture théorique dépendante de l'épaisseur et de l'élasticité de la glace a été comparée à la FSD. Sa corrélation avec la taille maximale indique que la banquise ne se fracture pas systématiquement à l'endroit où la déformation maximale se trouve comme il est assumé dans les modèles couplés d'interaction vague-glace. La demie longueur d'onde des vagues se propageant dans la glace fut aussi comparée à la taille maximale observée mais n'y est pas corrélée. Ces comparaisons laissent croire que la distance entre les craques est déterminée par l'épaisseur et la rigidité de la glace et non pas par les vagues.

Mots clés : Glace de mer, zone marginale, fragmentation, distribution de taille des floes

ABSTRACT

The marginal ice zone (MIZ) is a region of the ice pack characterized by its inner floe size variability and by its interaction with waves coming from the open ocean. Whether they are mechanical or thermodynamical in nature, the majority of processes taking place in the MIZ are dependent on floe size. Recent and dating observations of the spatial distribution of floe size (FSD) in the MIZ give a large scale portrait of its morphology which does not allow to understand the influence of each process on the shape of the FSD. The goals of this thesis are to observe the influence of wave-induced sea ice breakup on the shape of the FSD and to analyze the temporal evolution of this process. This will bring further the state of fundamental knowledge on the MIZ dynamics and will help to better represent floe size in models. It is thought that wave-induced breakup causes a preferential size but whether it is constrained by the flexural rigidity of sea ice or rather by the wavelength of the principal wave causing deflections in sea ice is still unknown from an observational point of view. To verify this hypothesis, two experiments were carried out : one in the gulf of Saint-Lawrence at winter 2019 and the other in Baffin bay at summer 2019, during which waves were generated by the *CCGS* Amundsen in order to generate break up in surrounding sea ice. The break up was recorded by a drone for the extraction of the FSD and of temporal properties. When represented as a probability density function, the FSD exhibits a strong modal shape which confirms the preferential size hypothesis. A theoretical fracture distance dependent on sea ice flexural rigidity (thickness, elasticity) was compared to the FSD. Its correlation with the maximum observed size indicates that sea ice does not systematically break up at the position of maximum strain as is assumed in wave-ice interaction models. Half the wavelength of the wave propagating in ice was also compared to the maximum size but it is not correlated to it. These comparisons seem to indicate that the distance between cracks is dictated by sea ice thickness and elasticity rather than by wave period or wavelength.

Keywords : Sea ice, Marginal Ice Zone, wave-induced sea ice breakup, floe size distribution

TABLE DES MATIÈRES

LISTE DES TABLEAUX

LISTE DES FIGURES

LISTE DES ABRÉVIATIONS

MIZ Zone marginale de glace (*Marginal Ice Zone*)

ATP Aéronef télépiloté

FSD Distribution de taille des floes (*Floes Size Distribution*)

PDF Densité de probabilité (*Probability Density Function*)

AFSD FSD prenant la forme d'une PDF calculée à partir de la surface des floes

NFSD FSD prenant la forme d'une PDF calculée à partir de la fréquence d'observation de la taille des floes

NGCC Navire de la guarde côtière canadienne

ND Number density

WIM Wave-Ice Interaction Model

UAV Unmanned Aerial Vehicle

GSL Gulf of Saint Lawrence

NBB Northern Baffin Bay

CCGS Canadian Coast Guard Ship

ODM Logiciel de traitement d'images Open Drone Map

DEM Digital Elevation Model

FSTD Joint Floe Size and Thickness Distribution

SAR Synthetic Aperture Radar

LISTE DES SYMBOLES

$n(d)$ nombre de floe en fonction de la taille

d Taille des floes

α Pente d'une décroissance exponentielle dans un graphique log-log

x^* Distance de fracture obtenue par la théorie de la flexion d'une poutre semi infinie reposant sur une fondation élastique

$D_{\mathbf{max}}$ Taille maximale engendrée par la fragmentation par les vagues dans les WIMs

$T_{\mathbf{air}}$ Température ambiante lors des expériences

Γ Critère isopérimétrique

A_i Aire du i ème floe

P_i Périmètre du i ème floe

a Axe majeur d'une ellipse correspondant à un floe

b Axe mineur d'une ellipse correspondant à un floe

θ Orientation de l'axe mineur par rapport à l'image

c_b Vitesse de fracture dans la direction de propagation des vagues dans la glace

c_p Vitesse de phase des vagues

f Fréquence des vagues

T Période des vagues

$\theta_{\mathbf{wave}}$ Angle des vagues mesuré visuellement dans l'expérience du GSL

λ Longueur d'onde des vagues mesurée visuellement dans l'expérience du GSL

λ^* Longueur d'onde théorique des vagues principales dans l'expérience NBB

$P(b_i)$ Probabilité associée à un axe mineur b_i

Δb Largeur des catégories de la PDF

n_i Nombre de floes ayant une taille entre b_i et $b_i + \Delta b$

Y Module de Young

Y_0 Module de Young pour de la glace d'eau douce

$Y*$ Module de Young effectif

ν_b Volume de saumure (*Brine Volume*)

U Vitesse du navire

ϑ Angle de propagation des vagues du navire

g Accélération gravitationnelle

ϕ_t Variation temporelle (t) du premier ordre du potentiel de vitesse (ϕ)

$\Delta\theta$ Différence d'angle entre la théorie et le pic de la distribution d'orientation des floes

η Niveau d'eau

a Amplitude des vagues

ω Fréquence angulaire

k Nombre d'onde

ε Déformation de la glace

h Épaisseur de la glace

P Pression exercée à l'extrémité de la glace

M Moment de flexion

E Module d'élasticité

I Moment d'inertie

k_f Module de fondation

ν Ratio de Poisson

ρ_w Densité de l'eau de mer

$g(\mathbf{x}, h, t)\, dh$ Probabilité de trouver de la glace ayant une épaisseur entre h et $h + dh$ à un moment t et à une position $\mathbf{x}$

$Q(d)$ Fonction de redistribution

$\beta(d_1, d_2)$ Redistributeur de la surface occupée par la taille d_1 vers celle occupée par la taille d_2

d_1 Taille initiale

d_2 Taille résultante de la fragmentation par les vagues

H Profondeur de l'océan

INTRODUCTION GÉNÉRALE

Dans le contexte actuel du réchauffement global, l'Arctique est la région la plus impactée avec une augmentation de température de surface dépassant le double de la moyenne planétaire (Overland et al., 2019). Cette augmentation a pour conséquence la réduction de la couverture de glace de mer estivale à un rythme de 10 % par décennie dans les 30 dernières années (Comiso et al., 2008). Une telle diminution de l'étendue de la banquise mène à une augmentation de la distance sur laquelle les vents peuvent exercer leur forçages, communément appelée *fetch*, générant ainsi des vagues de plus en plus énergétiques (Smith and Thomson, 2016; Stopa et al., 2016; Li et al., 2019; Casas-Prat and Wang, 2020) qui deviennent davantage susceptibles de briser la glace (Asplin et al., 2012; Thomson and Rogers, 2014). Non seulement les vagues sont-elles de plus en plus suceptibles de fracturer la glace de mer mais les tempêtes arctiques de plus en plus fréquentes (Rinke et al., 2017) contribuent aussi à briser la glace sur de grandes étendues. La réduction du couvert de glace de mer et sa fragmentation par le vent et les vagues ont des impacts sur plusieurs dimensions de la vie humaine, notamment sur le bien-être des communautés nordiques et sur l'accessibilité croissante de l'océan Arctique au transport maritime.

Le territoire des peuples Autochtones du Nord canadien possède non seulement un caractère géomorphologique grandiose, mais aussi une étonnante abondance de vie marine qui est intimement liée à la glace de mer (*siku* en Inuktitut) (Laidre and Regehr, 2016; Arrigo, 2016). Les veines d'eau de mer qui pénètrent cette portion du continent combinées à la topographie abrupte des côtes génèrent en effet des paysages à couper le souffle mais rendent tout autant difficile l'accès au territoire. Dans la région du *Nunatsiavut* (Labrador), les communautés sont souvent séparées par de grandes étendues d'eau et dépendent ainsi de la stabilité de la glace en hiver non seulement pour le transport entre les différentes municipalités, mais aussi pour la chasse et la pêche qui s'effectue souvent près de la marge de glace (*floe edge* en anglais ou *sinaa* en Inuktitut). La fragmentation de cette dernière par des groupes de vagues

d'autant plus énergétiques (Asplin et al., 2012) et fréquents (Rinke et al., 2017) ainsi que l'allongement de la saison de fonte (Markus et al., 2009) rendent précaire la relation entre les habitants de ces régions et leur environnement par la diminution de la période durant laquelle les activités de subsistance peuvent être effectuées en sécurité sur la glace. Cela résulte en une adaptation somme toute imposée qui a comme conséquences une prise de risque plus élevée lors de sorties sur la glace et l'emprunt d'itinéraires terrestres alternatifs qui produisent une usure prématurée des moyens de transports et, donc, un fardeau financier croissant (Kintisch, 2017). Au-delà de son aspect utilitaire, la glace de mer représente aussi une des pierres angulaires de la culture Inuit (Huntington et al., 2016). Malheureusement, la variabilité croissante du comportement de la glace fait en sorte que le transfert intergénérationnel de connaissances et de culture traditionnelle liées à celle-ci devient de plus en plus difficile (Krupnik and Jolly, 2002). Enfin, la fonte des glaces n'est qu'une infime portion de la déterioration générale du territoire des peuples Autochtones du Nord par les changements climatiques, détérioration qui génère un fardeau psychologique supplémentaire dans les communautés (Cunsolo Willox et al., 2012). Bref, non seulement les peuples Inuits ont-ils des fondations ébranlées par des décénnies de politiques colonialistes qui ont causé des déracinements socio-culturels, qu'ils vivent maintenant les conséquences d'un problème climatique auquel ils ont contribués que de façon marginale.

Une autre facette de la relation entre l'humain et l'Arctique est le transport maritime dans ces eaux qui, entre 1990 et 2015, a augmenté de près de 3 fois Dawson et al. (2018). L'utilisation du passage du Nord-Ouest, qui sillonne l'archipel arctique canadien, ou de celui du Nord-Est, longeant les côtes de la Sibérie, génère en effet une diminution de la distance de transit des navires comparativement à l'utilisation des canaux de Panama ou de Suez (Lasserre and Pelletier, 2011). Or, l'absence d'infrastructures essentielles au transport maritime dans cette région du globe et la variabilité des conditions de navigation associées à l'imprévisibilité de la dynamique de la glace de mer augmentent le niveau de risque et les coûts associés à la navigation commerciale dans l'océan Arctique, ce qui diminue la profitabilité du transport de ressources dans l'océan Arctique, voire l'engouement des compagnies à passer

par ces eaux (Lasserre and Pelletier, 2011). En fait, l'augmentation du trafic maritime dans l'Arctique entre 1990 et 2015 a été principalement générée par une augmentation de la circulation locale et dans une moindre mesure par le transport international (Dawson et al., 2018), augmentation qui illustre une interaction grandissante entre l'humain et l'environnement dans lequel la glace de mer morcelée se trouve.

Ceci dit, que ce soit pour les peuples Autochtones habitant les régions nordiques ou pour le transport maritime dans l'Arctique, l'interaction humaine dans les régions polaires est en grande partie dépendante de la connaissance du comportement de la glace mer et de la capacité à prédire sa dynamique. Par exemple, la connaissance *a priori* de la surface de glace affectée par un évènement de fragmentation par les vagues et du moment auquel ce processus sera déclenché dans une baie utilisée quotidiennement comme route serait un atout considérable permettant une meilleure gestion des risques pour les communautés. Du côté du transport maritime, savoir si une route sera encombrée ou non de floes de glace permettrait de rendre la navigation dans de telles eaux plus accessible et efficace. Une meilleure compréhension de la physique de la banquise pourrait également servir à mieux évaluer les impacts de la navigation dans des routes englacées utilisées par des communautés Inuit. Or, les modèles de prévision actuels n'ont pas la capacité de faire de telles prévisions, malgré le fait que des efforts croissants de recherche et de développement ont été réalisés en ce sens dans les dernières années.

À titre d'exemple, l'étude de Barrette et al. (2020) portant sur les climats régionaux des régions du *Nunavik* et du *Nunatsiavut* fait usage entre autres d'un modèle spectral de vagues, piloté par un ensemble de scénarios atmosphériques et par un modèle couplé glace-océan, pour estimer le risque de fragmentation de la banquise côtière par les vagues. Les résultats suggèrent que la période pendant laquelle il est sécuritaire d'accéder à la banquise diminuera d'environ 30 jours en 2050, et d'environ 100 jours en 2100 sur les côtes du Nunavik bordant la Baie d'Hudson. Ce nouvel indicateur de l'impact des changements climatiques peut être évalué seulement si la physique des interactions vagues-glace est représentée dans

ces modèles.

D'un point de vue physique, lorsque la glace est morcelée par de grands vents ou par des groupes de vagues, sa dynamique – autant thermique que mécanique – ainsi que son interaction éventuelle avec les vagues évolue. En mettant en contact plus de surface latérale de glace avec l'eau de mer, c.-à-d. en augmentant le périmètre total, la fragmentation déclenche une boucle de rétroaction dont l'issue sera déterminée par la température ambiante. À un mercure sous -2°C [2], les ouvertures d'eau générées entre les floes gèleront pour ainsi augmenter l'étendue gelée alors que dans des conditions tempérées, la surface latérale des floes étant exposée à l'eau et à l'air fondra pour ainsi diminuer la couverture de glace initiale (Asplin et al., 2012). Ceci dit, plus les morceaux fragmentés auront une petite taille, plus la surface latérale et le périmètre totaux seront grands et, donc, plus le gel ou le dégel associés seront importants (Steele, 1992). Dans le cas d'un regel, la création d'une nouvelle plaque de glace à partir de plusieurs floes soudés ensemble changera la réponse de l'étendue gelée à une contrainte externe. En effet, la résistance au mouvement d'une plaque de glace étant plus grande que celle de plusieurs petits floes qui couvrent la même étendue (Rothrock and Thorndike, 1984) fait en sorte que l'augmentation, ou la diminution, de l'étendue de glace de mer issue de la rétroaction thermodynamique – qui elle même est dépendante de la taille des floes – aura un impact sur le comportement mécanique de la banquise.

À grande échelle, l'étendue de glace fragmentée soumise à l'action des vagues – communément appelée la zone marginale de glace (MIZ pour *marginal ice zone*) – se déforme spatialement avec souplesse lorsque soumise à une contrainte mécanique externe comme celles qui peuvent être générées par le vent, les vagues et les courants (Rothrock and Thorndike, 1984; Dumont et al., 2011). La banquise interne, qui se trouve à l'abri de la majorité des vagues en étant entre la côte et la MIZ, possède quant à elle une rigidité provenant d'une grande cohésion horizontale issue du fait qu'elle est constituée de grandes plaques de glace

2. Pour de l'eau de mer à des valeur de salinité usuelles entre 30 et 35 PSU

possédant des étendues de l'ordre de la centaine de kilomètres (Roach, 2019). Cette partie de la banquise joue le rôle de condition initiale pour la zone marginale, car c'est la fragmentation par les vagues et les vents qui morcelera les grandes plaques de glace pour alimenter la MIZ en fragments de glace de toutes tailles, allant du centimètre au kilomètre d'envergure. Ceux-ci seront ensuite advectés par les vents et les courants marins. Leur morphologie sera influencée thermodynamiquement par la fonte et le gel latéraux, et mécaniquement par l'abrasion, la fracture thermique et par des évènements de fragmentation subséquents (Rothrock and Thorndike, 1984). La nature *granulaire* de la MIZ laisse place à une cohésion horizontale faible, voire nulle, et rend ainsi sa dynamique advective similaire à celle d'un fluide (voir Fig. 1). Ce comportement mécanique complètement différent de celui de la banquise interne met en valeur le fait que la réponse advective d'une étendue de glace à une contrainte externe dépend de la taille des floes qu'elle contient.

Il a été mentionné qu'en étant derrière la MIZ, la banquise interne est d'une certaine façon à l'abri des vagues mais pourquoi est-ce le cas ? Pour répondre à cette question, il faut s'attarder à comment la structure tridimensionnelle des vagues se fait modifier par la présence de morceaux de glace à la surface de l'eau. En fait, en se propageant dans la zone marginale, les vagues transfèrent d'abord leur énergie cinétique aux floes de glace en les mettant en mouvement. Cette énergie est ensuite diminuée par différents mécanismes de dissipation et par la diffraction. De façon générale et

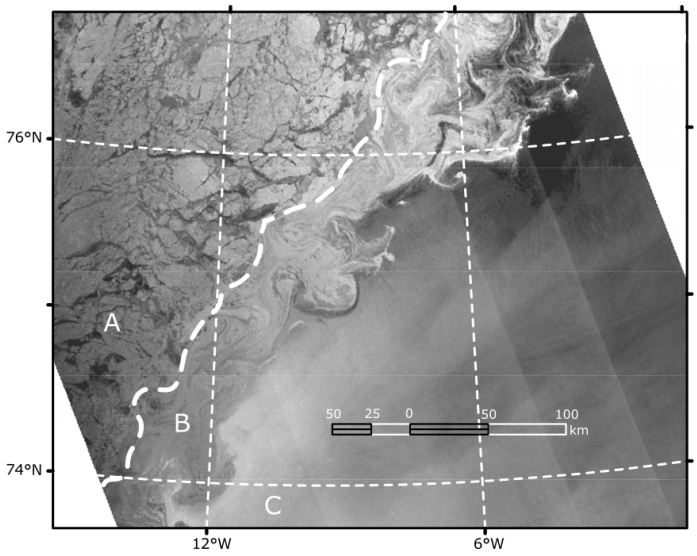

Figure 1: Image radar à synthèse d'ouverture prise par un stellite de l'agence spatiale européenne le 16 janvier 2010 qui montre une partie de la banquise arctique hivernale le long du détroit de Fram. On y voit la zone marginale de glace (B) qui est située entre l'océan (C) et la banquise interne (A). Tiré de Dumont et al. (2011).

faiblement simplifiée, cela mène à une atténuation exponentielle de l'amplitude des vagues en fonction de la distance parcourue par celles-ci dans la MIZ et à leur redistribution directionnelle (Masson and Leblond, 1989; Squire, 1995, 2018) – voilà donc comment la banquise interne est protégée de la majorité des vagues. La présence de glace à la surface de l'océan agit aussi comme un filtre passe-bande en laissant passer seulement les fréquences qui sont propres à l'oscillation naturelle de la glace tout en réflétant ou en atténuant très rapidement celles qui ne répondent pas à ce critère (Fox and Squire, 1991; Kohout and Meylan, 2008). Dans certaines études récentes visant à inclure la taille des floes dans la modélisation à large échelle (e.g. Roach, 2019), l'atténuation des vagues est modélisée comme étant dépendante du nombre de floes rencontrés par les vagues. Cette démarche est basée sur l'hypothèse que l'énergie des vagues est réfléchie de façon linéaire à chaque fois qu'elle rencontre un changement d'impédance, ce qui permet au principe de superposition de s'appliquer. La réduction de l'amplitude du champ de vagues ne semble toutefois pas directement dépendante de la taille des floes (Kohout and Meylan, 2008; Bennetts et al., 2010), mais le fait qu'elle dépende de leur nombre indique une dépendance indirecte sur la taille car, pour une surface donnée, il est possible d'avoir plus de floes de petite taille que de grands.

À la lumière des paragraphes précédents, on comprend que la dynamique de la MIZ dépend de la taille des floes, que ce soit par des processus thermiques comme la fonte latérale, dans son comportement advectif ou par son interaction avec les vagues. Or, dans les modèles climatiques contemporains – ceux qui peuvent par exemple servir à prédire l'année où l'océan arctique ne sera plus couvert de glace de mer – ainsi que dans les modèles de prévisions opérationnels, la taille des floes n'est soit tout simplement pas considérée ou l'on y attribue seulement une valeur constante afin de paramétrer la fonte latérale (Roach, 2019), sans plus. Étant donné que la banquise pluriannuelle de l'Arctique est progressivement remplacée par une glace de mer saisonnière (Comiso et al., 2008) de plus en plus influencée par les vagues (Asplin et al., 2012; Smith and Thomson, 2016), il serait pertinent– vu les multiples processus qui dépendent de la taille des floes qui y prennent place – de considérer la dimension horizontale des floes dans les équations qui régissent l'évolution temporelle de la banquise.

Il faut toutefois être réaliste, l'ajout si fondamental d'une variable indépendante dans les modèles numériques nécessite une compréhension profonde de la dynamique de la zone marginale et une traduction mathématique de celle-ci étant capable de ressembler à la réalité lorsqu'introduite dans un contexte de modélisation ; savoirs et application dont la communauté scientifique s'attardant à la glace de mer ne possède pas complètement.

Bien sûr il y a, d'un côté, l'angle théorique et mathématique du développement de la connaissance fondamentale et son application dans le but d'améliorer les prévisions. Or, celles-ci sont indissociables de la sphère observationnelle qui met à l'épreuve les théories et qui fourni les éléments nécessaires à leur raffinement ou à leur remise en question pour en développer de nouvelles. Quel est donc l'état des connaissances scientifiques observationnelles sur la taille des floes dans la zone marginale ? Afin de répondre à cette question, il nous faut introduire le concept de distribution de taille des floes (FSD pour *floe size distribution*) : une variable servant à caractériser la morphologie de la glace sur une étendue donnée. Pour l'obtenir, on délimite dans une image – soit manuellement ou à l'aide d'un algorithme – le contour du plus grand nombre de floes possible pour ensuite les compter et obtenir leur propriétés géométriques. On utilise ensuite un des paramètres morphologiques, comme par

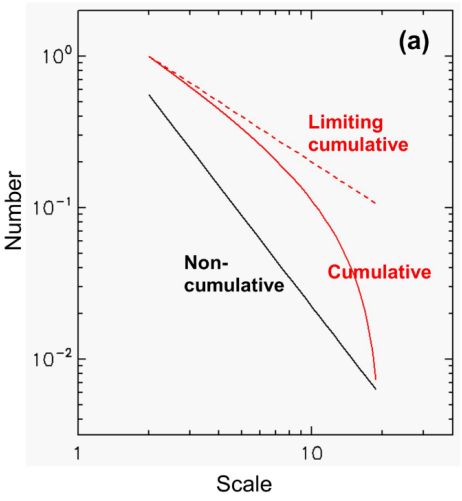

(a)

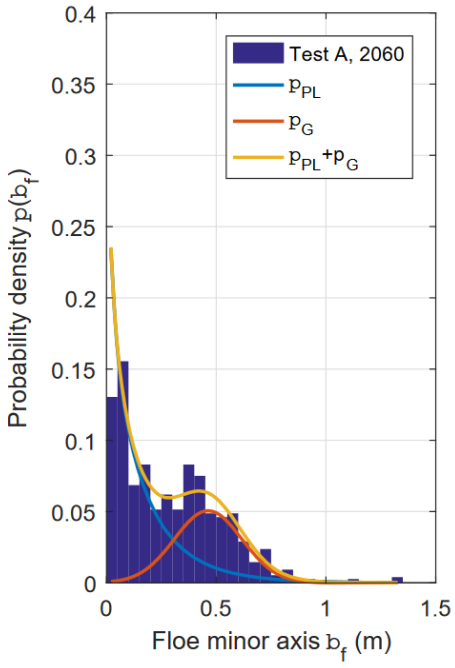

(b)

Figure 2: Représentations actuelles de la FSD dans la littérature scientifique : soit comme **(a)** une *number density* (Fig. 1 de Stern et al., 2018b) ou comme **(b)** une densité de probabilité (Fig. 7e de Herman et al., 2018).

exemple le diamètre, pour définir ce qui sera utilisée comme *taille* dans la distribution de *taille* des floes. Deux approches existent pour représenter cette dernière : soit le nombre total de floes en fonction de la taille sera tracé sous forme de courbe de façon à créer ce qu'on appelle une *number density* (voir Fig. 2a) ou soit des probabilités d'occurence basées sur la fréquence d'observation seront associées à des classes de grandeur pour créer une *densité de probabilité* qui prendra la forme d'un histogramme (voir Fig. 2b). La première méthode est la plus couramment utilisée dans les études observationnelles sans vraiment avoir un avantage quelconque sur la seconde (Stern et al., 2018b). Ces études observationnelles sur la FSD, ayant été réalisées dans les zones marginales arctique et antarctique (e.g. Weeks et al., 1980; Rothrock and Thorndike, 1984; Holt and Martin, 2001; Toyota and Enomoto, 2002; Toyota et al., 2006, 2011; Stern et al., 2018a), concluent que lorsqu'influencée par tous les processus physiques prenant place dans la MIZ, celle-ci – quand représentée sous la forme d'une *number density* – suit la forme d'une loi de puissance (*power law*) dont l'expression mathématique est une décroissance exponentielle s'écrivant comme $n(d) = d^{-\alpha}$ où n est le nombre de floes, d est la longueur caractéristique des floes et α est la pente de cette décroissance dans une échelle logarithmique. L'état actuel des connaissances observationnelles sur la FSD dans la zone marginale est donc un portrait général qui aide à comprendre la morphologie de la MIZ à large échelle, mais qui laisse encore un voile d'incompréhension sur comment les processus sous-jacents influencent la forme de la distribution de taille.

Comme ces observations sont les seules actuellement disponibles et que plusieurs scientifiques différents sont parvenus au même résultats, les modèles spectraux d'interactions vague-glace ont utilisé – et utilisent encore – la loi de puissance comme référence et la convertissent en densité de probabilité pour ensuite paramétrer différents processus, notamment la fragmentation de la glace par les vagues, sur celle-ci (Dumont et al., 2011; Williams et al., 2013a,b; Zhang et al., 2016; Bennetts et al., 2017; Boutin et al., 2018; Bateson et al., 2019; Boutin et al., 2020). Un point important à comprendre ici est que la forme de la densité de probabilité utilisée a une incidence sur le résultats des paramétrisations que l'on fait des processus. Par exemple, certains d'entre eux dépendent d'un moment statistique de cette

distribution comme la taille moyenne ou de son aire sous la courbe à cause du fait qu'une intégration numérique est nécessaire pour l'obtention du résultat. Dans un monde idéal, l'expression mathématique exacte de chacun des processus physiques serait incluse dans les modèles de sorte que la forme de la FSD évoluerait de façon réaliste en suivant la physique de la zone marginale. Or, les observations disponibles actuellement ne peuvent donner des informations spécifiques quant à l'influence de chacun des processus sur la FSD, car elles traduisent uniquement un portrait général de celle-ci. Il est donc impossible pour le moment de décrire mathématiquement la contribution réelle de chacun des phénomène à la FSD à part leur donner une règle basée sur l'intuition. Ainsi, vu l'influence grandissante des vagues sur la banquise, les lacunes au niveau de l'intégration de la taille des floes dans les modèles et l'absence d'observations de l'influence des vagues sur la forme de la FSD, j'ai décidé, pour ma maîtrise, d'étudier la fragmentation de la glace de mer par les vagues sous un angle observationnel afin de pallier à ces manques dans la communauté scientifique.

À travers ce mémoire, le thème de la fragmentation de la glace de mer par les vagues est abordé dans un contexte expérimental unique et novateur qui saura répondre à ce besoin observationnel spécifique. C'est à l'aide du *NGCC Amundsen* et d'un aéronef télépiloté (ATP) que des évènements de fragmentation de glace de mer on pu être simulés par les vagues du navire et enregistrés grâce à la caméra de l'ATP à la fois dans le golfe du Saint-Laurent (GSL) et dans le nord de la baie de Baffin (NBB). Les images recueillies par l'ATP, lorsque soumises à du traitement d'image, offrent la possibilité d'obtenir des FSD issues *directement* de la fragmentation et, donc, de cibler l'influence de ce processus sur la distribution de taille des floes. De plus, une nouvelle façon de construire la densité de probibilité est proposée dans ce mémoire, laquelle diverge de l'utilisation du nombre de floes, ou de la fréquence d'observation, pour plutôt se diriger vers celle du ratio entre la surface des floes et l'étendue imagée afin d'établir la probabilité d'occurence des classes de taille. On comprend que ces résultats représentent les principales contributions scientifiques du mémoire par le pont qu'ils permettent de faire entre la sphère des observations et celle de la modélisation. Le contexte méthodologique utilisé pour cette maîtrise est une première dans le millieu observationnel de

la glace de mer et permet donc non seulement d'obtenir des informations sur la taille des floes résultante de la fragmentation par des vagues, mais aussi sur l'évolution temporelle du processus lui-même, chose qui était impossible auparavant vu la faible résolution temporelle des satellites ou la sporadicité des observations aériennes. L'analyse de l'évolution des propriétés des vagues lors de leur pénétration dans la glace ainsi que l'obtention de la vitesse de fracture sont les points saillants des résultats obtenus pour la dimension temporelle de l'étude.

ARTICLE 1

OBSERVATIONS AÉRIENNES DE LA FRAGMENTATION DE BANQUISE PAR DES VAGUES DE NAVIRE

1.1 Résumé en français du premier article

La zone marginale de glace (MIZ) est une région de la banquise caractérisée par la variabilité de la taille des morceaux de glace (floes) qui la composent et par sa forte interaction avec les vagues. Une grande quantité de processus se produisant dans cette partie de la banquise ont un impact sur la taille des floes. Toutefois, les observations actuellement disponibles qui concernent la distribution de la taille des floes (FSD) dressent un portrait général, à large échelle, de la morphologie de la MIZ ne permettant pas de comprendre la contribution de chacun des processus à la modification de la FSD. Ici, deux évènements de fragmentation en milieu naturel ont été simulés à l'aide d'un navire et enregistrés par un aéronef télépiloté (ATP) dans le but principal de comprendre l'influence de la fragmentation par les vagues sur la forme de la FSD et secondaire d'obtenir de l'information sur l'évolution temporelle de ce processus. Deux orthomosaïques ont été générées à partir des enregistrements de l'ATP et ont ensuite été traitées soit de façon manuelle ou à l'aide d'un algorithme automatisé afin d'obtenir la FSD. Une nouvelle approche, laquelle est basée sur la surface des floes (AFSD) plutôt que leur nombre (NFSD), pour construire la densité de probabilité est proposée dans cet article. Dans les 2 expériences, les AFSD exhibent une forme modale ce qui indique qu'une taille préférentielle est générée par la fragmentation. Celle-ci semble augmenter avec l'épaisseur de la glace mais la variabilité de la vitesse du navire entre les deux expériences, et donc de la longueur d'onde des vagues incidentes, empêche d'attribuer le déplacement du mode uniquement à l'épaisseur. Une distance de fracture théorique dépendante de la rigidité flexurale de la glace a été comparée à la taille maximale des AFSD. Elle y est correllée ce

qui semble indiquer que la glace ne se fracture pas systématiquement à l'endroit où la déformation maximale se trouve malgré le fait que plusieurs cycles de vagues sont nécessaires à la fragmentation.

L'article qui est présenté dans ce mémoire, s'intitulant "*Aerial observations of sea ice break up by ship-induced waves*", fut co-rédigé par moi-même, par les professeurs Dany Dumont et Daniel Bourgault ainsi que par mon collègue Jérémy Baudry. L'article sera soumis dans la revue *Journal of Geophysical Research : Oceans* dès lors qu'une révision complète et finale sera effectuée par tous les rédacteurs. En tant que premier auteur, ma contribution à ce travail a été de faire la revue de littérature sur l'état de l'art de la recherche dans le domaine de la glace de mer fragmentée, de planifier et d'exécuter les missions de terrain en mer, de faire le traitement et l'analyse des données, d'apporter des idées novatrices quant à la direction du projet de recherche et de rédiger l'article. Dany Dumont, second auteur, a joué un rôle crucial dans la planification des activités de recherche et a fourni l'idée originale qui est le fondement de ce projet : utiliser un navire pour simuler la fragmentation de la banquise en milieu naturel. Il a aussi soutenu le projet dans son ensemble et corrigé le mémoire. Jérémy Baudry, troisième auteur, a amené des idées originale quant à l'analyse et à l'interprétation des données. Et pour finir, le quatrième auteur, Daniel Bourgault, a lui aussi aidé à la correction du mémoire pour le mener à sa version finale.

1.2 Introduction

The marginal ice zone (MIZ) is the ice-covered region found between the open ocean and the inner ice pack that is affected by waves and that keeps extending as a consequence of a warmer climate (Horvat and Tziperman, 2015; Squire, 2020). In the current context of global warming, negative trends in both Arctic sea ice thickness and summer extent are observed (Kwok and Rothrock, 2009; Cavalieri and Parkinson, 2012). The summer minimum extent has been decreasing at a rate of 10% per decade over the last 30 years (Comiso et al., 2008) which consequently provides greater fetch to increasingly frequent cyclones (Rinke et al., 2017) that further generate more energetic wave fields in the Arctic basin (Smith and Thomson, 2016; Stopa et al., 2016; Li et al., 2019; Casas-Prat and Wang, 2020). Hence, sea ice becomes increasingly prone to interact with surface waves (Asplin et al., 2012; Thomson and Rogers, 2014) so that the overall dynamics of the ice pack is changing. Numerous physical processes, including wave attenuation by sea ice floes, wave-induced sea ice breakup and lateral melt take place in the MIZ and depend either directly or indirectly on the size of sea ice floes.

By fracturing large pieces of sea ice into smaller ones, waves change the floe size distribution (FSD) locally and contribute to the increase of the total lateral sea ice surface being in contact with water. This results in a greater total sea ice perimeter and in the exposure to the atmosphere of water areas that were previously capped under a layer of sea ice. Depending on ambient weather conditions, such an exposure can either lead to enhanced surface melt due to a smaller overall albedo, trigger a higher rate of lateral melt due to the increase in perimeter (Steele, 1992), or to enhanced ice formation due to a negative flux of heat from the ocean to the atmosphere. In addition to thermal feedbacks, the FSD has an impact on large scale sea ice dynamics, more precisely on the way it deforms and drifts under external stresses (Dumont et al., 2011). The presence of ice floes at the surface of the ocean also impacts the propagation of incoming waves and their generation in the MIZ (Masson and Leblond, 1989). By scattering and dissipating energy, ice floes attenuate and redistribute directionally the am-

plitude of the wave field in a manner that is thought not to depend directly on floe size but rather on their number within a given area (Squire, 1995; Kohout and Meylan, 2008; Bennetts et al., 2010; Squire, 2018). Hence, by impacting the size of ice floes and other morphological aspects of the ice-covered ocean, wave-induced break-up triggers multiple processes and feedbacks which have a direct impact on the MIZ dynamics and possibly an influence on climate.

Given the importance of floe size in sea ice dynamics, there is a need to collect FSD observations in the MIZ; the major portion of which comes from satellite or aerial imagery of the arctic and antarctic MIZs (Weeks et al., 1980; Rothrock and Thorndike, 1984; Holt and Martin, 2001; Toyota and Enomoto, 2002; Toyota et al., 2006, 2011; Lu et al., 2008; Herman, 2010; Alberello et al., 2019). After identifying the boundaries of individual ice floes in the images by using either autonomous image processing algorithms or manually, a characteristic length scale, such as the mean caliper diameter (e.g. Rothrock and Thorndike, 1984), is determined and then used as *floe size*. The FSD is then represented either as a number density (ND) or as a probability density function (PDF). The former approach, which is widely used while not having any particular advantage on the second, takes the form of a continuous curve relating the number of floes per square kilometres to the floe size in a cumulative or non-cumulative way (see Figure 1 of Stern et al., 2018b). In the second approach, categories of floe size are being attributed a probability of occurrence based on the frequency of observation in order to represent the FSD as an histogram (see Figure 7 of Herman et al., 2018). It appears from the above-mentionned studies that when represented as a ND, the FSD generally follows a power law of the form $n(d) \propto d^{-\alpha}$ where n is the number of floes having a characteristic floe size d. This type of distribution has been tied to the fractal and possibly invariant nature of fractured sea ice (Rothrock and Thorndike, 1984), presented as a path for understanding the broad characteristics of underlying physical processes. A review of the available FSD observations and of the power law topic is made by Stern et al. (2018b). In the end, these observations give a large scale view of the MIZ morphology and can give information on the seasonal evolution of the FSD. However, both the low temporal

resolution of satellite images and the sparseness of aerial observations do not allow to capture individual breaking events. This limits our understanding on how the FSD within a particular MIZ arises from wave-induced break up; crucial knowledge for the development of realistic parametrizations in wave-ice interaction models (WIMs).

Large-scale spectral WIMs (Dumont et al., 2011; Williams et al., 2013a,b; Zhang et al., 2016; Bennetts et al., 2017; Boutin et al., 2018; Bateson et al., 2019; Boutin et al., 2020) use the power law as a reference for the FSD in order to estimate sea ice morphological properties such as the mean floe size. Such statistical moments are dependent on the shape of the FSD and are further used to parametrize numerous MIZ processes, namely wave-induced break up. Such a use of the power law FSD, and the parametrizations that come with it, allows to study the consequences of the insertion of a FSD on modelled sea ice dynamics, which is a good step towards the inclusion of the FSD in global climate models. But, by simplifying and idealizing how MIZ processes affect the shape of the FSD, these models do not represent a physically-based solution of the MIZ dynamics (Herman, 2017). For example, Dumont et al. (2011), Williams et al. (2013a), Williams et al. (2013b), Boutin et al. (2018), Bateson et al. (2019) and Boutin et al. (2020) all model the influence of breakup on the power law-distributed FSD as an update of the maximum floe size ($D_{\max}$) while there is no empirical evidence that this is really how fragmentation affects the shape of the FSD. To our knowledge, Roach et al. (2018) made the first global wave-ice interaction modelling effort which did not impose a particular form to the FSD but rather let it evolve according to thermal and mechanical processes similarly to what is proposed by Horvat and Tziperman (2015). By assuming that ice breaks up where the deformation is maximal, Roach et al. (2018) obtained that the fracture of sea ice by waves leads to a preferential size. This means that wave-induced break up leads to a modally shaped FSD, a result which indicates that the morphology of floes resulting from breakup might not be well represented by a power law as it is made in WIMs.

Focusing on the break-up itself rather than on its influence on dynamics, Fox and Squire

(1991) studied the propagation of strain into an ice sheet. Modelling sea ice as a thin, semi-infinite elastic plate, they obtained that "*the position [of maximum strain] depends crucially on ice thickness and to a lesser extent on wave period*". On the other hand, Herman (2017), by modelling the ice cover as a strip of discrete cubic-shaped grains being linked by elastic bonds, obtained that "*breaking of a continuous ice sheet by waves produces floes of almost equal size, dependent on thickness and strength of the ice but not on the characteristics of the incoming waves*". Hence, despite using different frameworks and assumptions, Herman (2017) and Fox and Squire (1991) have come to the same conclusion that not only floe size resulting from wave-induced break up does not depend on the spectral structure of the ocean waves but rather on sea ice thickness and rigidity but also that a preferential size is created by this mechanism. Hence, from a process-based modelling point of view, the FSD resulting from wave-induced break does not follow a power law but rather a modal distribution as a preferential size is obtained. However, the question remains as to whether these theoretical conclusions are supported by field observations.

Although there has been significant efforts to model the break-up process, only few studies have approached the problem from an observational perspective (e.g. Langhorne et al., 1998; Kohout et al., 2014). Furthermore, little attention has been put towards the analysis of the resulting FSD and its possible connexion to sea ice thickness and rigidity. The first anecdotal observations of wave-induced breakup are recalled in a review of the wave-ice interaction topic by Squire (1995). Therein, he states that "*the width of the strips [...] created by the process is remarkably consistent and appears [...] to be rather insensitive to the spectral structure of the sea but highly dependent on ice thickness*". In other words, he observed that the distance between successive cracks generated by break up seems to be constant and independent from the sea state but rather dependent on the material properties of sea ice. This remark supports qualitatively well the conclusions of Fox and Squire (1991) and Herman (2017) but quantitative analysis are required to fully test these hypotheses. More recently, Herman et al. (2018) carried out break up experiments in large tanks where a waves were generated artificially to break apart a layer of laboratory-grown ice with the goal of testing

Herman (2017) and Squire (1995) conclusions on the independence of the break up pattern on wave properties. Herman et al. (2018) compared the mean sizes obtained from the experiments to a theoretical fracture distance x^* derived by Mellor (1983) which is dependent on the flexural rigidity of the material considered, in this case ice, but not on wave period or length. For a group of experiment (group A), the value of x^* was close to the mean size so that Herman et al. (2018) concludes that *"the floe size resulting from breaking by waves depends not on the incoming wavelength, but rather on the mechanical properties of the ice itself"*. In other words, it means that waves produce floes that are anisotropic and that the minor axis of these floes is independent of the wavelength. Unfortunately, a factor of $\frac{1}{2}$ was omitted in the mathematical expression of x^* (as demonstrated in Sec. 1.6.3.3) so that this conclusion needs to be revisited. With that in mind, observations of sea ice break up by waves in the natural environment could help test the flexural rigidity-dependent preferential size hypothesis and to better understand the overall FSD generated by this process. Determining such details from observations would help to develop physically-based parameterizations of wave-induced break up in WIMs.

Few studies about break up have been made yet mainly because the MIZ is an arduous area to sample directly from. It is indeed hard to be in the MIZ at the right place and at the right time, with good but not too harsh weather conditions for break up to happen, and with the right apparatus to measure all relevant variables during a natural break up event. Indeed it is possible to study wave-ice interactions in laboratories as Herman et al. (2018) did, but it is not clear if the results directly apply to the natural environment due to the scaling of the apparatus used and of the properties of laboratory-grown sea ice. Because the occurrence of sea ice break up by wind-generated sea surface waves is hard to predict, a ship was used here jointly with an unmanned aerial vehicle (UAV or drone) with the primary goal of quantifying the FSD resulting from the breakup of sea ice plates in the natural environment. Secondly, we wanted to observe the temporal evolution in order to assess a fracture timescale relative to wave propagation and to see if wave properties are being modified by the presence of ice at the surface. Two experiments were conducted, one in the Gulf of St. Lawrence (GSL) during

winter and the other, during summer in Northern Baffin Bay (NBB). The UAV recorded high resolution footage of both the temporal evolution of breakup and images of the resulting ice fragments. Ice thickness was also measured in order to correlate it to the FSD.

1.3 Methods

A UAV was deployed from the Canadian Coast Guard Ship (CCGS) *Amundsen* in order to acquire high resolution footage of broken sea ice by ship-generated waves. Such a combination hands a better management of weather conditions for drone deployments while still allowing to study break-up in the natural environment. The use of a ship also allows to have no constraint on the location of deployments and to search for the right sea ice to break, i.e. a vast plate of level ice that has at least one of its side exposed to a wide area of open water.

A DJI Mavic 2 Pro was used for both experiments because of its autonomy, resilience to cold temperature, hovering stability and high resolution 20 Mpx Hasselblad camera. This UAV is equipped with a 3-axis gimbal which reduces noise from the video recordings. The camera has a 65.5° field of view (FOV), a 5472 $\times$ 3648 pixels resolution in capture mode and a 3840 $\times$ 2160 pixels resolution in video mode. While its height relative to the takeoff location is obtained by a barometric sensor, it uses both GPS and GLONASS geopositioning systems to locate itself, hover in a still position and correct its altitude, with vertical and horizontal precisions of 0.5 and 1.5 m, respectively.

Two experiments were carried out, the first one in February 2019 in the GSL and the second in August 2019 in NBB. In both experiments, no waves nor swell were present, hence the observed break-up can only be attributed to ship-generated waves.

1.3.1 Gulf of St. Lawrence

The first opportunistic experiment was conducted in the northwestern Gulf of St. Lawrence (GSL), Canada, at (49.584°N, 66.152°W) on February 7 2019 during clear sky conditions and air temperature of $T_{\text{air}} = -7.2$°C. According to the ice chart produced by the Canadian Ice Service (CIS) on 7 February 2019, the ice concentration was 9+/10 and the ice thickness was between 10 and 30 cm as grey and grey-white ice were identified to be the most present ice types.

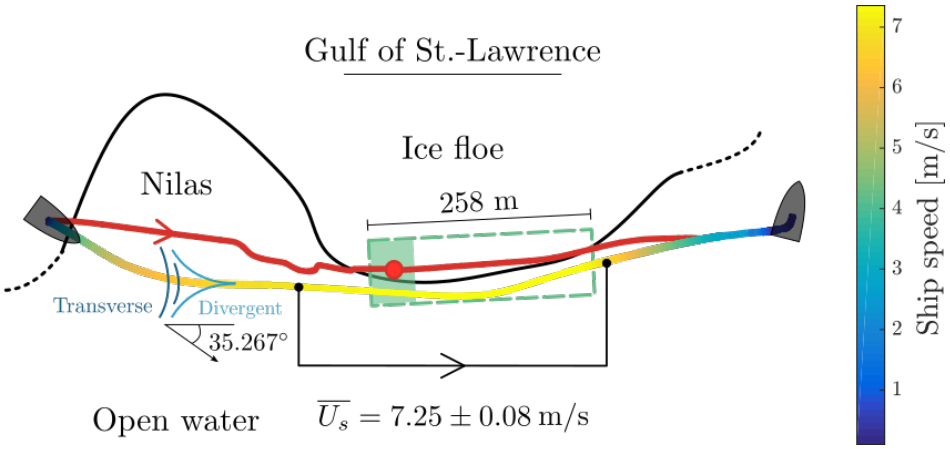

Figure 3: Visual description of the experiment made in the GSL. The open water area was covered by a thin layer of nilas.

For this experiment, the *CCGS Amundsen* accelerated to an average speed of 7.25 ± 0.08 m/s at less than 50 meters from the initial floe edge, thereby generating a wave train with enough energy to break up surrounding sea ice (see Figure 4). The error on the speed value was assessed by taking one standard deviation of the speed distribution above 7 m s^{-1}; threshold at which the ship starts to decelerate and to have a speed close to constant. Figure 3 shows the setup of the GSL experiment. The red line indicates the drone's GPS path and the blue to yellow line is the ship's GPS track. The red dot is the position at which the drone recorded the live break up event while the green area is its FOV. Lighting conditions allowed the visual evaluation of flexural wave properties (wavelength, period and direction) from brightness variations in the video footage and thus to obtain information on the transient

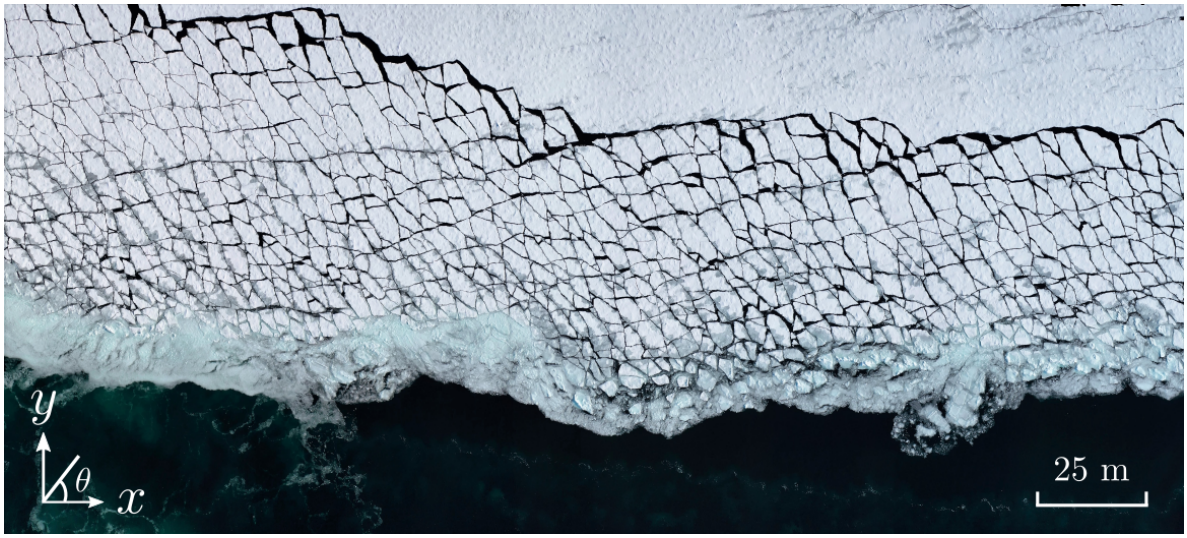

Figure 4: Breakup resulting from the GSL experiment.

evolution of break up (see section 1.5.1). The green dashed rectangle is the approximate span of the mosaic of broken sea ice shown in Figure 4 which was acquired as the drone flew back from the recording site to the ship and filmed the broken ice. Using the drone's mean altitude of 94.7 ± 0.5 m and its field of view, a metric conversion factor of 3.1 cm px^{-1} was obtained. Note that the error on that value, caused by the variation of the drone's altitude, is of the order of 0.01 cm px^{-1} and is thereby considered as being negligible. By combining the orthomosaic, the metric conversion factor and image processing methods, the FSD resulting directly from wave-induced breakup was obtained. Unfortunately, no apparatus capable of measuring the waves was deployed on the ice nor in the water during the experiment, leaving us with only visual approximation of wave properties in ice and with first order theoretical values for those in water.

1.3.2 Northern Baffin Bay

The second experiment was conducted in northern Baffin Bay (NBB) at (77.883°N, 77.341°W) on August 5 2019 in cloudy conditions and with air temperature of T_{air} = 4.9°C.

According to the ice chart produced by the Canadian Ice Service (CIS) on this day, ice concentration was 4/10 and the ice thickness was identified to be between 30 and over 120 cm as thin and thick first year ice were indicated to be present. The floe chosen for the experiment consisted in a plate of heavily rotten first year ice of about 540-m wide and more than 2-km long. The thickness was assessed on some floes resulting from the experiment using a meter stick and was measured to be between 40 and 60 cm.

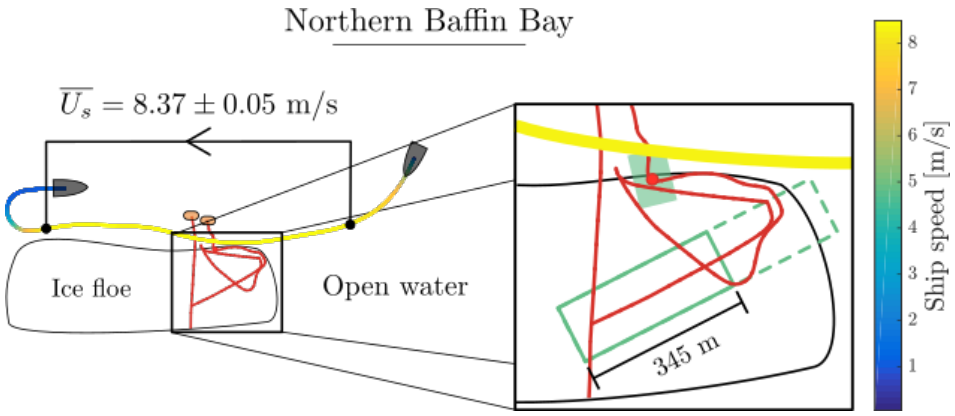

Figure 5: Visual description of the experiment made in the NBB.

The *CCGS Amundsen* accelerated to an average speed of 8.37 ± 0.05 m/s at less then 50 m from the isolated sea ice floe thereby generating breakup (see Figure 6). The uncertainty on ship speed is based on the same metric than for the GSL experiment. Similarly to Figure 3, Figure 5 describes the experimental setup made in the NBB. Note that the green dashed rectangle is the approximate span of the whole transect of broken sea ice taken with the UAV while the green solid rectangle is the extent considered for the analysis, i.e. Figure 6. In this experiment, an attempt was made to deploy wave buoys on the ice with a zodiac boat – represented as an orange polygon in Figure 5 – before waves hit and fractured the floe. Two SKIb buoys (Guimarães et al., 2018) were put within 2 to 3 m of the floe edge with a long stick as it was not possible to go on the ice floe, and spaced roughly 10 m apart from each other in order to measure the wave period. Next, the zodiac boat took a safe distance from the ice floe and the UAV was then flown to the ice edge in order to record the temporal evolution of the process. Shortly after the recording was started, heavy overwash caused by the ship

waves made the buoys flip on their side and roll, making their data unusable. Moreover, the propagation of flexural waves in the ice floe could not be observed visually like it was possible in the GSL experiment due to a lack of contrast caused by flat lighting conditions. In ice wave properties thus could not be obtained neither from in situ nor remote sensing measurements during this experiment. Next, the UAV was flown while taking pictures at an interval of 2 s to recreate a partial map of the broken floe, which was made with the use of the open source software Open Drone Map (ODM). By having in hand pictures rather than footage of broken sea ice – as was the case for the GSL – for this experiment, geographical coordinates of each floe could be estimated by ODM to generate a georeferenced map of broken sea ice at a resolution of 5 cm px^{-1} (see Figure 6). A flight pattern was also made with the intent of recreating a digital elevation model (DEM) of the broken sea ice which would have allowed to obtain the first data set on the joint floe size and thickness distribution (FSTD). Unfortunately, sea ice drifted and thus it was impossible to generate the DEM.

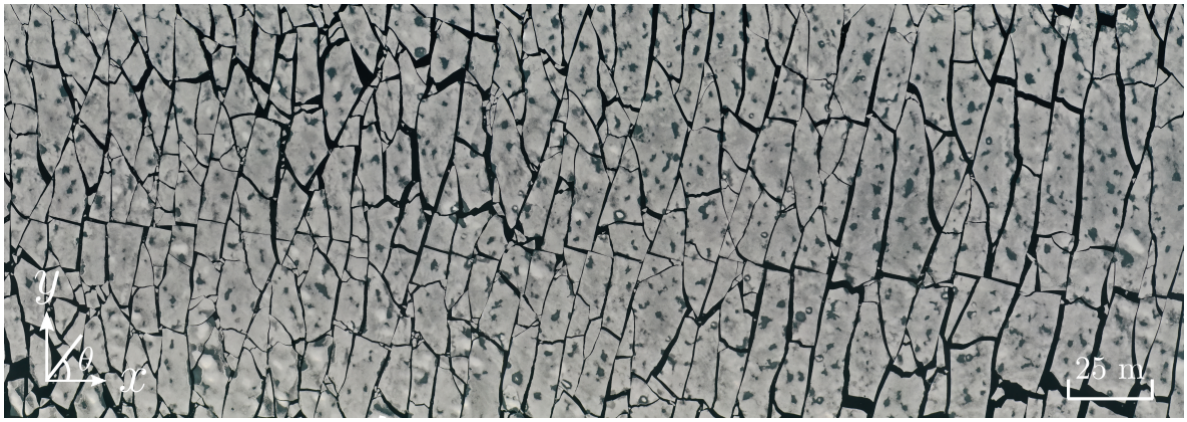

Figure 6: Partial view of the breakup resulting from the NBB experiment.

1.4 Image processing

1.4.1 Obtaining transient properties

The speed of the break-up front was evaluated using an automated and unsupervised algorithm which identified the furthest fracture point along transects oriented in the wave's propagation direction (colored areas in Figure 7). The algorithm first initializes polygons in the wave direction that span the initial unbroken sea ice cover and then calculates, every 0.2 s, the position of the furthest pixel having a brightness under 90/255. This intensity threshold was adjusted manually in order to optimize the fidelity of the algorithm to follow cracks at the right pace. It is then by taking the slope of the linear regression relating fracture distance to elapsed time that the breakup speed is assessed.

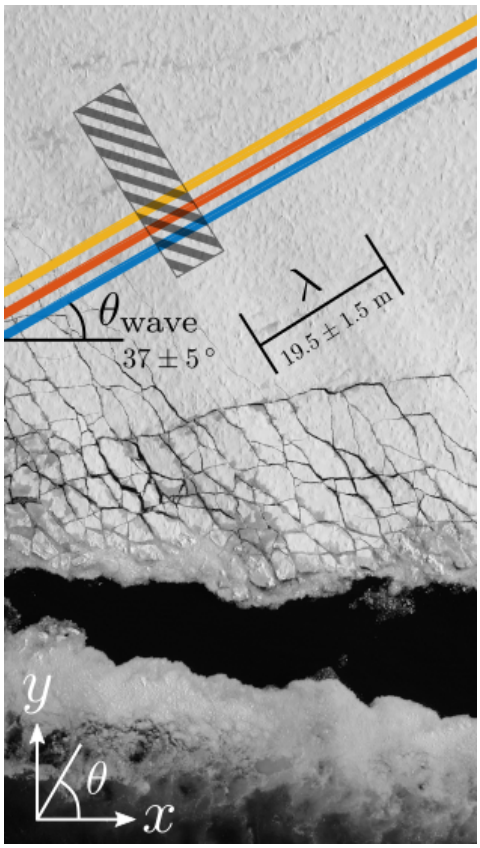

Figure 7: FOV of the drone while recording the breakup in the GSL. The colored lines indicate the polygons used to calculate the breakup speed while the dash-filled rectangle is the ROI used for the estimation of wave period. The *x*-*y* axes are the coordinate system of the image from which floe and wave orientations are defined.

Combined with the wavelength that could be measured manually in the GSL experiment (see Figure 7), an estimation of the period allowed the computation of the wave's phase speed. In order to do such an estimation, a region of interest (ROI) is first selected manually and then each 0.2 s the mean brightness of this ROI is recorded. A Fourier transform is then applied to the resulting signal in order to obtain the wave period. The ROI (dashed rectangle in Figure 7) was chosen to be oriented along with the wave's direction of propagation and to have a along-wave size of less than half a

wavelength so that brightness variations induced by the waves could be efficiently captured.

1.4.2 Floe boundary detection

The identification of sea ice in camera footage consists in a series of steps that are illustrated in Figure 8. It starts with the simple conversion of the image from RGB to grayscale. Next, an intensity threshold is applied to the brightness histogram of the image in order to create a first binary map. That way, pixels with brightness greater than the threshold are considered as ice and are given a value of 1 while those lower than the threshold are considered as water and are given a value of 0. Numerous flaws are present in this first binary map. First, *slushy* ice between multiple floes can have a brightness above the threshold which leads to their merge into one single piece of ice. Moreover, artificial holes in ice can be generated by the presence of dirt, shaded areas on sea ice due surface roughness and melt ponds because of their low brightness which would generate water pixels. That said, calculating morphological properties of the floes contained in the first binary map does not represent well those of the original image. In order to counter such flaws, a second identification of sea ice called segmentation is made by applying intricate image processing methods on the first binary map. A lot of methods for sea ice segmentation, such as morphology gradient (Zhang et al., 2012), watershed transform (Meyer, 1994; Zhang et al., 2013) or gradient vector flow (Zhang and Skjetne, 2014, 2015), have been developed and tested but all of them

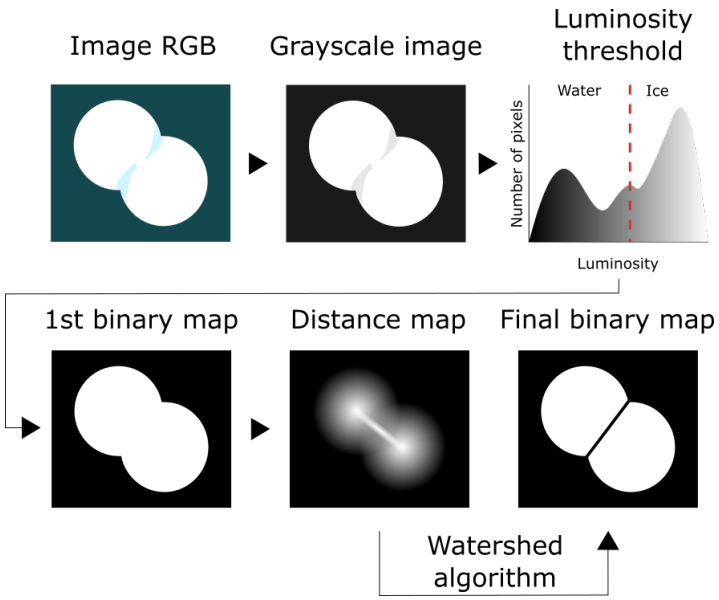

Figure 8: Steps of the image processing algorithm used for the boundary identification of floes in the GSL experiment.

have pros and cons. A good review of sea ice image processing methods and literature is done by Zhang and Skjetne (2018).

In our case, the best method is the watershed transform algorithm described in detail by Meyer (1994) and illustrated in Figure 8. In short, it uses the Euclidean distance transform of the first binary map generated as a topography map in order to erect watersheds which correspond to individual floes. However, this method has flaws such as generation of initially non-existent floes, under-segmentation and over-segmentation (Zhang and Skjetne, 2018) but it is possible to circumvent these issues with fine adjustments. To counter over-segmentation, local minima in the distance transform were withdrawn and, for under-segmentation, successive morphological erosion and dilation of floes boundary were made in order to separate floes which were previously linked together. Another source of error coming from the watershed transform method is that it generates odd-shaped floes within other floes. As these floes have a very high perimeter to surface ratio, an isoperimetric criterion $\Gamma = \frac{P^2}{4\pi A}$, where P is the floe perimeter and A is its area, was used to remove them. A threshold value $\Gamma_c = 3.5$ was found to be the best in order to get rid of aberrant floes.

Figure 9: Sample of the ellipses fitted on the ice floes by Maltab. Blue lines indicate the major axes (a) and yellow ones show the minor axes (b).

Similarly to Herman et al. (2018), it was also chosen to remove sea ice floes having a horizontal dimension close to their thickness since they are not directly generated by flexure. In the case of the GSL experiment, floes having a surface of less than 900 cm^2, corresponding to a thickness of 30 cm for a perfectly square floe, were removed as for the NBB experiment, floes having their area under 3600 cm^2, corresponding to a thickness of 60 cm, were removed.

In the end, a thorough visual examination of the resulting binary map for the GSL experiment shows that it corresponds well to the initial image and that morphological properties of sea ice floes can be extracted from it. For the NBB experiment, the omnipresence of large melt ponds at the surface of the floes made it impossible to detect efficiently sea ice boundaries using the watershed transform method so the images were manually segmented. The filtering methods made for the GSL experiment were also applied on NBB's binary map in order to have coherence regarding the methodology and to set the same baseline of analysis.

By fitting an ellipse to each floe present in the final binary maps, Matlab's *Image Processing Toolbox* allows to get numerous morphological properties of sea ice floes. Those of interest here are the major axis a, the minor axis b and angle θ. The orientation of floes is calculated to be the angle of their minor axis relative to the x axis shown in Figure 9. That way the angle of floes are comparable to the angle of the ship-generated waves. The elongation of floes, defined as the ratio between its major and minor axes, will also be used to discard circular floe that could have an erroneous angle value attributed to them. Following Squire (1995) and Herman et al. (2018), the minor axis length is considered here to be the floe size since it is a measurement of the distance between successive cracks, i.e. the length scale created by wave-induced break up.

1.5 Results

1.5.1 Transient properties

The break up evolution, partly shown in Figure 10, was measured to have a speed of 1.97 ± 0.04 m s^{-1} in the GSL experiment, with the error corresponding to the 95% confidence interval of the linear regression (see Figure 11). This speed is equal to 39.4% of the wave phase speed c_p which means that it takes on average the passage of 2.54 wave crests to change the position of the ice edge in this experiment.

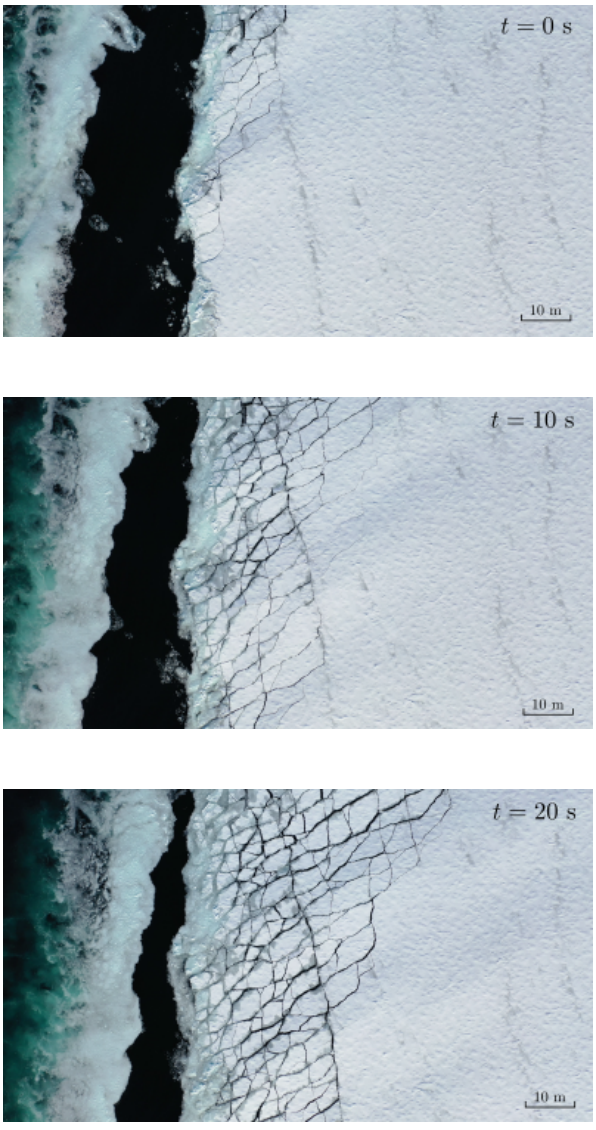

Figure 10: Portion of the breakup's temporal evolution. The presence of *slushy* ice can be seen at the ice edge, defined as the boundary where open water and broken sea ice meet.

Figure 12 displays the temporal evolution of the ROI's mean brightness (left panel) and the power density spectrum (PSD) corresponding to its Fourier transform (right panel). The latter has a peak frequency at $f = 0.25 \pm 0.01$ Hz, which is equivalent to a period $T = 4.0 \pm 0.2$ s. The uncertainty of these values account for the error associated with a finite sampling time interval of the mean brightness. Both the angle, $37 \pm 5°$, and wavelength, 19.5 ± 1.5 m, of the wave propagating into unbroken sea ice have been measured manually using Matlab's *Image Processing Toolkit* (see Figure 7). The error attributed to these measurements

account for the maximum and minimum values that could be possibly manually measured.

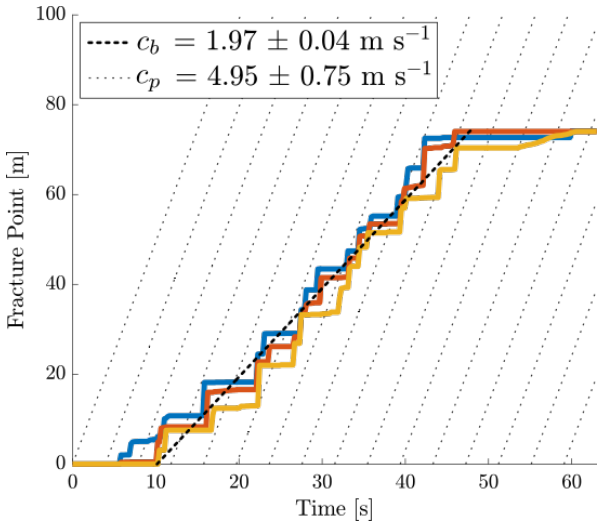

Figure 11: Temporal evolution of the fracture position relative to the $x = 0$ boundary of the colored polygons in Figure 7. Dotted lines indicates position of wave crests while the bold dashed line is the linear regression.

As no in-ice wave properties could be sampled in the NBB experiment, the first order linear Kelvin ship wake theory was used to approximate a wave angle (see Appendix 1). Using the latter theory, GPS tracks and compass headings of both the ship and the UAV, a value of 19 ± 4 ° was computed and assigned to the angle of propagation of the maximum amplitude waves in the images coordinates of Figure 6. Hence, the theoretical angle of propagation for maximum amplitude waves of 35.264° (Soomere, 2007) was subtracted from the mean ship heading and then the latter was compared to the mean drone heading to get a value relative to the x-axis in Figure 6. The error on the resulting angle value comes from the fact that the trajectory of both the ship and the UAV were not following a straight path, thus one standard deviation of the heading distributions was used as the uncertainty.

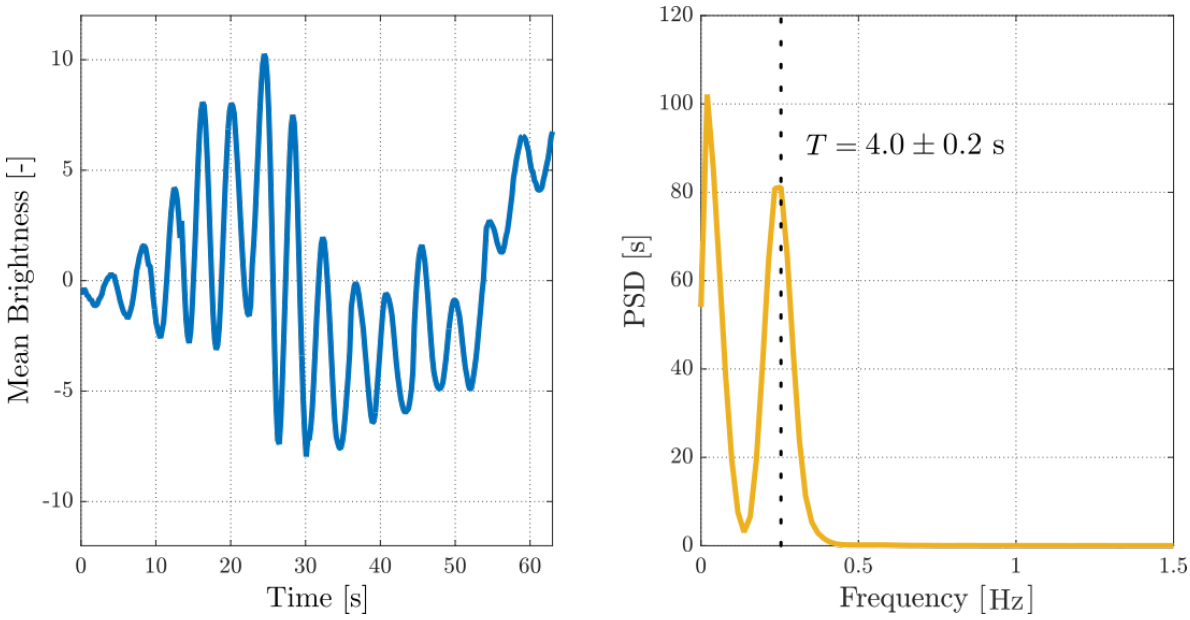

Figure 12: (Left) Temporal evolution of the detrended mean brightness of the ROI described in section 1.5.1. (Right) The corresponding Fourier transform.

1.5.2 Resulting break-up

In the GSL, fracture penetrated up to 60 m from the ice edge leading to a partial break-up of the floe. For the NBB experiment, the entire plate – which had an average lateral dimension of 540 m – was broken-up by the ship-generated waves. Figure 4 shows the breakup that has been captured by the UAV shortly after the passage of the ship (along the x-axis) in the GSL. Figure 6 only displays a part of the breakup that happened during the NBB experiment as the ice floe was too big to be sampled in its whole. Both of these images exhibit the presence of preferential sizes and fracture angles but also show presence of a great range of shapes and orientations.

The elongation and orientation are represented as histograms and a PDF is used to show the distribution of minor axis values, i.e. the FSDs, for both experiments. The normalization required by going from an histogram to a PDF ensures that the shape of the FSDs does not change with the number of bins. The latter was calculated by rounding upward the square root

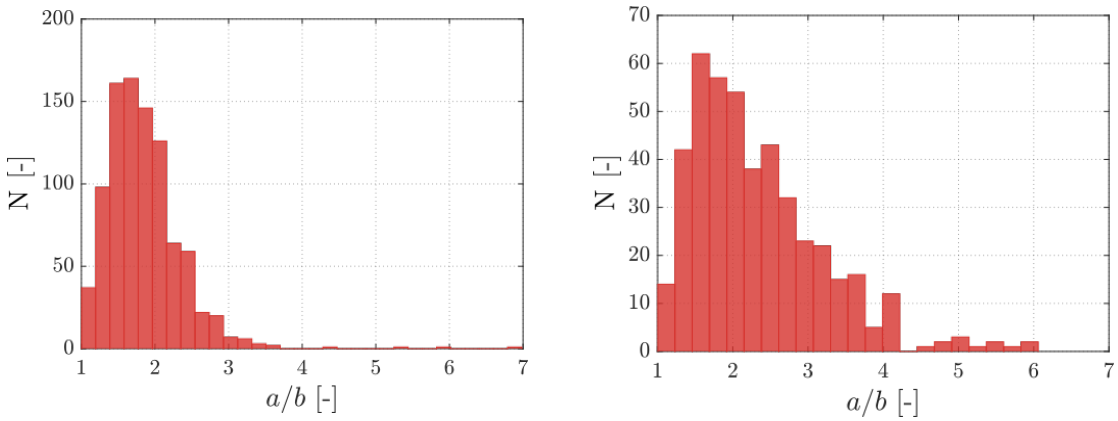

(a) GSL (b) NBB

Figure 13: Histogram of the number of floes as a function of their major-to-minor axis ratio for both experiment.

of the number of floes sampled in the images. Bin width is set as a constant and is calculated by dividing the range of floe size by the number of bins. For an in-depth discussion about the binning of the FSD and the PDF normalization, see (Stern et al., 2018b).

Figure 13 shows the floe elongation, i.e. the major to minor axis ratio, distribution for the GSL and NBB experiments. Floes with elongations less than 1.4 were not considered for further analysis. This was done in order to discard fragments that are too close to being a circle, i.e. with an elongation equal to 1, and for which the angle could be ambiguously determined. This threshold value is considered to be the most appropriate to remove the wrongful angle measurements, and to keep as much sea ice floes as possible for analysis.

Figure 14 presents histograms of the floes orientation for the GSL and NBB experiment. The GSL distribution is Gaussian-like having a mean of 47.4° and a standard deviation of 21.3°. The peak value for GSL is of 41.6° which lies between the uncertainty of with the visually measured direction of the wave, i.e. $\theta_{\text{wave}} = 37 \pm 5°$. For the NBB, the shape is also modal, with a mean value of −2.4°, but more scattered with a standard deviation of 25.2°. The peak value for NBB is located at 1.3° which is, in this case, far from the theoretical value

of 19 ± 4 °.

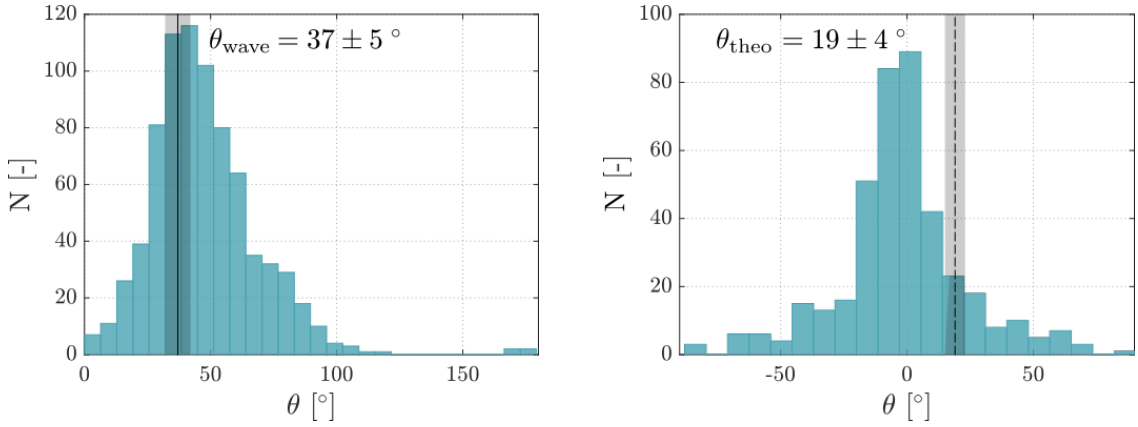

(a) GSL (b) NBB

Figure 14: Angle distribution of floes having an elongation greater than 1.4 for both experiments. The measured wave angles and their uncertainty ($37 \pm 5°$ and $19 \pm 4°$) are respectively plotted as lines and shaded areas. The reference angle for NBB is dashed to symbolize the fact that it is not a measurement but rather an estimation based on theory.

Figure 15 (a-b) shows the number based probability density function, i.e. the NFSD, for both experiment. Here, only floes having an elongation greater than 1.4 and an angle within one standard deviation of the mean value of their respective angle distributions are considered. The latter condition is made to remove the floes that do not follow the preferential orientation. This allows the selection of floes which were broken up by the deflection caused by wave-induced flexure. The GSL NFSD exhibits a strong modal shape at a mean value of 2.8 m with a standard deviation of only 1.2 m. For the NBB, The NFSD has a bimodal signature with a mean value of 5.9 m and a standard deviation of 3.4 m. On the other hand, Figure 15 (c-d) display the unfiltered NFSD for the GSL and the NBB experiments respectively in order to illustrate how low sized floes are removed by the application of the elongation and angle filters. It is interesting to see that the unfiltered NBB FSD as a shape similar to what Herman et al. (2018) obtained in a laboratory wave-induced ice fracture experiment (more precisely in test A 2060 of Herman et al. (2018)) that is the sum of a power-law and a gaussian distribution. When looking at the orthomosaics of broken ice resulting from

the two experiments (Figure 4 and Figure 6) there is a clear dominance of floes of a certain size which is indeed well represented for the GSL by the modal shape seen in Figure 15a. Nonetheless, the weak modal signature at high sizes in both the filtered and unfiltered NBB NFSD shows that what is seen in the NBB orthomosaic is not well rendered by the NFSD. Hence, the area of floes should be used in order to construct the probability density function in order to obtain an adequate portrait of the recording.

1.5.3 Using the area of floes to calculate their probability of occurrence

When estimating a PDF from the number of floes, the probability $P_N(b_i)$ associated to the i^{th} size category is calculated using the following

$$P_N(b_i) = \frac{n_i}{N\ \Delta b}, \qquad \sum_i P_N(b_i)\Delta b = 1 \tag{1.1}$$

where N is the total number of floes, n_i is the number of floes within the i^{th} size category and Δb is the bin width. Another way to compute the PDF is to combine the ratio of each floe's surface to the total area of sea ice in the image thus yielding an area-based probability noted $P_A(b_i)$ so that

$$P_A(b_i) = \frac{1}{\Delta b} \sum_{j=0}^{n_i} \frac{A_j}{\sum_{k=0}^{N} A_k}, \qquad \sum_i P_A(b_i)\Delta b = 1 \tag{1.2}$$

where A_j is j^{th} floe surface. Figure 16 shows the AFSDs obtained by calculating the probabilities of occurrence with eq. (1.2) for both the GSL and NBB experiments. By comparing Figure 15d and Figure 16b to Figure 6, it is clear that the area-based method is better than the number-based one to represent adequately the preferential size signature seen in Figure 6. Indeed this new approach gives more weight to the large floes, which are prominent but not abundant in the orthomosaic, and attributes less importance to the smaller ones, which cover a small extent of the image but which are frequently observed, so that the preferential signa-

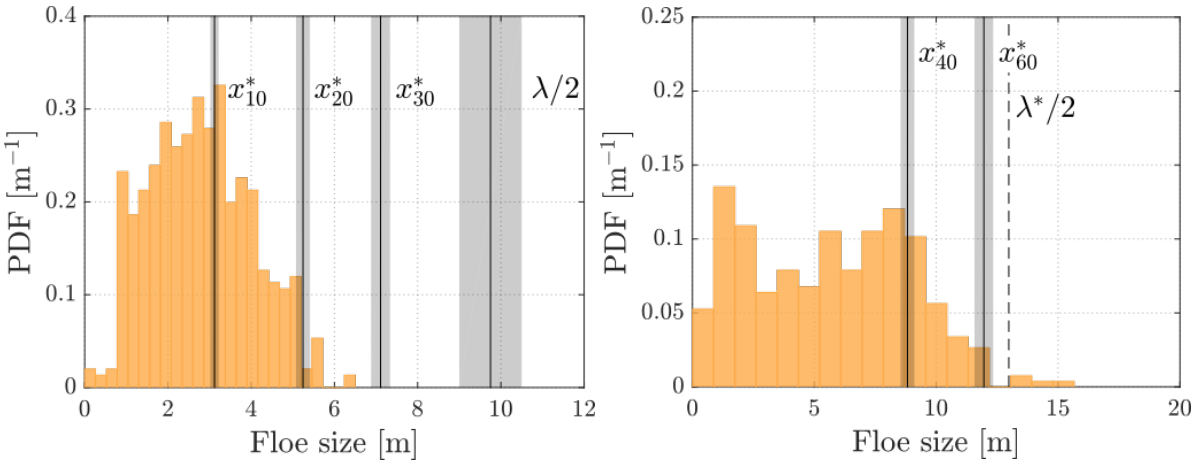

(a) GSL (b) NBB

(c) GSL Unfiltered (d) NBB Unfiltered

Figure 15: Number-based probability density functions of floe size (NFSDs) resulting from the breakup experiments of (a - b) floes having an elongation greater than 1.4 and an angle within one standard deviation of the mean orientation and of (c - d) all floes. λ is the in-ice wavelenght measured in the GSL, λ^* is the inferred wavelength using 0.866 $\times$ Eq. (1.4) and x^* is calculated with Eq. (1.10), gray bars indicate uncertainties.

ture is better represented. Relative to Figure 15a, Figure 16a shows only a slight translation of the mean to higher values. It is worth noting here that no criterion was used to filter the floes during the computation of Figure 16.

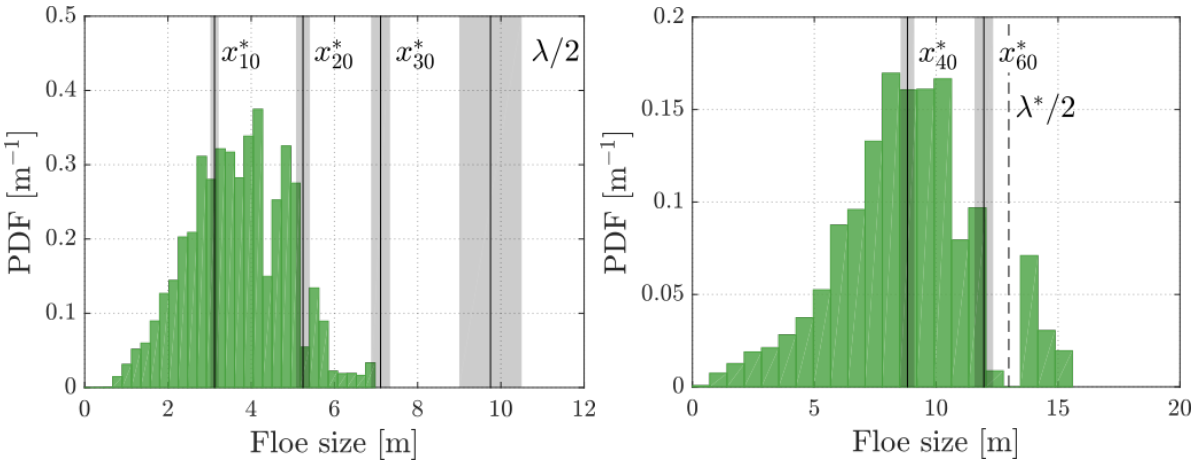

(a) GSL (b) NBB

Figure 16: Area-based probability density functions of floe size (AFSDs) resulting from the breakup experiments calculated with eq. (1.2). Both half of wavelength and Mellor's fracture criterion x^* are presented, gray bars indicate uncertainties. All floes were considered for the computation of this figure.

1.6 Discussion

1.6.1 Span of fracture

The difference in breakup extent between the two experiments is thought to be attributable to the following causes : 1) the difference in ship cruising speed, 2) the difference in brine volume contained in sea ice and 3) a possible thickness-driven preferential deformation of sea ice. In the GSL experiment, the ship has kept a stable speed of 7.25 ± 0.08 m s^{-1} during the breakup while in the NBB experiment, it was of 8.37 ± 0.05 m s^{-1}. Such an increase results necessarily in a higher wave energy input as more water is displaced by the ship in the same time interval. A more intricate modelling of the ocean surface structure caused by a moving ship in deep waters using a 3-D model of the *CCGS Amundsen* could lead to a quantification of the impact of a difference of 1.12 ± 0.13 m s^{-1} in ship speed on the energy of the maximum amplitude wave but such an analysis is out of the scope of this paper.

The brine volume was not measured directly during the experiments but it is still possible to make assumptions regarding the relative brine content of sea ice between the experiments using its state and ambient weather conditions. In the GSL, grey and grey-white ice were evolving in a freezing weather conditions ($T_{\text{air}} = -7.2°\text{C}$) while the ice present for the NBB experiment consisted in heavily rotten first year ice which was in weather which favored melting ($T_{\text{air}} = 4.9°\text{C}$). Hence, it would be reasonable to assume that the brine volume, i.e. the volume of salty melt water contained into sea ice, has been higher in the NBB sea ice than in the GSL sea ice. Timco and Weeks (2010) have found that the resistance of sea ice to elastic deformations, i.e. its Young's modulus, follows a linear relationship with brine volume

$$Y = Y_0(1 - 3.51\nu_b) \quad \text{[GPa]} \tag{1.3}$$

where Y_0 ($\sim$ 10 GPa) is approximately the value for freshwater ice at high loading rates (Williams et al., 2013a) and ν_b is the brine volume expressed in decimal values (i.e. a value of 0.05 will be used if the brine volume is 500 ppt). Hence, the more brine is contained into sea ice, the less it will resist to deformations and the more it will deform under a stress. Based on the fact that a higher deformation leads to greater strains in the ice, it seems logical that the heavily rotten sea ice floe used in the NBB experiment broke at a greater extent than what was observed in the GSL.

Another possible cause for the difference of breakup penetration is the resonance frequency, or period, of the ice. As exposed by Fox and Squire (1991), the strain profile caused by waves of a given period penetrating sea ice depends on sea ice thickness. Not only the amplitude of the peak strain value but also its position are affected by ice thickness for a given period (see Figure 3 of Fox and Squire (1991)). Hence, the difference between the wave frequency which penetrated the ice plate and the natural resonant frequency of the sea ice may have been smaller in the NBB experiment than in the GSL experiment, thus causing a more strenuous strain field in the ice which led to a larger depth of breakup.

That said, no quantification of each proposed contributors to the larger breakup extent can be made here. Still, it leaves us knowing that the wave field energy, the melting state of sea ice and the resonance between sea ice and waves might have a positive impact on sea ice breakup extent and that these factors may well be taken into account when modelling this phenomenon.

1.6.2 Evolution of the wave through ice

In order to see if wave properties could be affected by a change in the sea surface nature, theoretical values for wave period, wavelength and phase speed of the waves generated by the ship were computed using the theory of Thomson (1887) (see Appendix 1) and then compared to observations made in the GSL. Inserting the average ship speed of the stable speed regimes and the angle of propagation of the maximum amplitude waves, i.e. 35.264 ° (Soomere, 2007), in the following equations

$$\lambda(U,\vartheta) = \frac{2\pi U^2}{g}\cos^2\vartheta, \quad T(U,\vartheta) = \frac{2\pi U}{g}\cos\vartheta. \tag{1.4}$$

respectively gives values of 22.5 m, 3.8 s and 5.9 m s^{-1} for wavelength, period and phase speed for the GSL experiment. Note that the derivation of Eqs. (1.4) is based on the assumption that the wave velocity potential is stationary, i.e. $\phi_t = 0$ (see Appendix 1). This corresponds to cases where no ambient waves are present, which was the case for both experiments, or where the ship is sailing at a constant speed. Figures 3 and 5 show that a steady-state approximation seems realistic for both the GSL and the NBB experiments as the ship speed was stable when sailing in the vicinity of sea ice.

The reduction in wavelength and phase speed of waves by going from water through ice in the GSL experiment (see Table. 1) suggests that sea ice, for relatively low thicknesses (10 to 30 cm), lowers the speed and wavelength but does not affect the period; a result which is coherent with what was observed by Liu and Mollo-Christensen (1988) at a larger scale. It is

Table 1: List of the observed and theoretical values of transient and angular properties of waves for both experiments. The observed floe orientation is also indicated for reference.

	Gulf of St. Lawrence (GSL)		Northern Baffin Bay (NBB)	
	Observation	Theory	Observation	Theory
λ [m]	19.5 ± 1.5	22.5	–	29.9
T [s]	4.0 ± 0.2	3.8	–	4.4
c_p [m s^{-1}]	4.9 ± 0.6	5.9	–	6.8
c_b [m s^{-1}]	1.97 ± 0.04	–	–	–
θ_{wave} [°]	37 ± 5	35.3	–	19 ± 4
$\overline{\theta_{\text{ice}}}$[°]	47.4	–	1.3	–
$\theta_{\text{ice}}\big\vert_{\max(N)}$ [°]	41.6	–	−2.4	–

interesting to see that there is no notable difference in the angle of propagation of the waves, which is counter intuitive when compared to standard refraction. For the NBB experiment, where ice was thicker (40 to 60 cm), transient properties could not be measured but the relationship between the angle of propagation of waves and the angle of fracture of sea ice floes is different than what was observed in the GSL since a significant change ($\Delta\theta = 21.4 \pm 4°$) has been measured between these two. Three causes could be responsible for this discrepancy : (i) the change of the direction of propagation of waves in the ice, (ii) the presence of a preferential angle of fracture driven by thickness, and (iii) the uncertainty on the incident wave direction due to the curved ship trajectory as it approached the floe. The latter is considered as being the most probable reason. The fact that the ship did not follow a straight path while accelerating generated a wave system that had energy traveling in multiple directions. The theoretical *maximum amplitude wave angle* might not be 35.264° in this case and so the theoretical angle of 19 ± 4° might not be an adequate reference.

Another key quantity obtained in the GSL experiment is the breakup speed. Being a small but yet significant fraction of the wave phase speed in ice, the breakup speed ob-

tained here leads to the conclusion that fragmentation could be assumed to be instantaneous in coupled spectral WIMs such as those developed by Dumont et al. (2011), Williams et al. (2013a,b), Boutin et al. (2018) and Bateson et al. (2019) if the time step is greater than a minute and if the resolution is of the order of 100 m.

1.6.3 Floe size distribution

1.6.3.1 Note on image processing

The spatial distributions of the minor axis of floes resulting from breakup — the FSDs — have here been represented by PDFs which were either weighted by the frequency of observation or by the surface of the floes. The comparison of the shapes of the GSL and NBB FSDs obtained with the number-based approach leads to the conclusion that the watershed method used for the GSL data does not represent adequately low floe sizes but still gives a trustable result for the modal size which can be seen in Figure 4. This is explained by the fact that the action of smoothing the distance map by removing local minima, action which prevents oversegmentation, leads to a loss of resolution in the minimum identifiable floe size. Small floes, by being close to each other, hence being related to low amplitude distance maps, are thus more prone to be merged together to create larger floes.

The fact that no reliable algorithm for sea ice boundary detection exists limits sea ice observational research. At the moment, an amount of time equal to – or even higher than – manually segmenting can be spent on tuning the parameters of segmentation algorithms. Hence, the use of state-of-the-art algorithms does not really benefit users. A lot of work has been made into making practical algorithms for both satellite Synthetic Aperture Radar (SAR) and visible imagery (see sec. 2 of Hwang et al. (2017)). But, an algorithm based on deep learning being able to cope with a wide range of ice types and resolutions while not demanding too much parameter sensitivity analysis is certainly needed. That way, new and precise observational data which could help to bring further sea ice modelling could be

efficiently obtained.

1.6.3.2 Observational evidence of thickness-dependent preferential floe size ?

As was mentionned in the introduction, some authors have found evidence that a preferential size, which depends solely on sea ice flexural rigidity and not wave structure, is generated by wave-induced break up (e.g. Squire, 1995; Fox and Squire, 1991; Herman, 2017). The shape of the AFSDs obtained in our experiments show that a preferential size is indeed produced by the fragmentation of sea ice by waves as the distributions exibhit a modal shape. The mean value of the AFSD increases with higher thicknesses since it went from 3.57 m in the GSL with $h_{\mathrm{GSL}} \in [10, 30]$ cm, to 9.00 m in the NBB with $h_{\mathrm{NBB}} \in [40, 60]$ cm. Whether this favored length depends or not on wave structure cannot be determined since the speed of the ship, and thus wavelength and amplitude of the principal wave, was different in each experiment. Hence, it is not possible to confirm the conclusion of Squire (1995), Fox and Squire (1991) and Herman (2017).

1.6.3.3 Comparison of the AFSDs with flexure theories

Flexural break-up in WIM is parameterized considering that waves propagate instantaneously across an ice floe (see Figure 4 of Dumont et al., 2011). It further considers that the sea level η beneath the ice follows a sinusoïdal curve, i.e. $\eta = a\sin(\omega t - kx)$. The flexural strain ε at given time for a monochromatic wave propagating axially into the ice is therefore

$$\varepsilon = \frac{h}{2}\frac{\partial^2 \eta}{\partial x^2} = -\frac{k^2 h}{2}\sin kx. \tag{1.5}$$

Taking the first-order derivative of eq. (1.5) and equaling it to zero gives the location of strain extrema, which here are separated by a distance $\lambda/2$ (Dumont et al., 2011). Thus, by assuming that the ice will break last where the peaks of deformation are, the maximum floe

size $D_{\max}$ to be possibly generated by the process will have a length of $\lambda/2$. This approach is very computationally effective as it allows WIM to go from a wave spectrum directly to a floe size distribution.

Another way to view the bending of sea ice under the propagation of surface waves is to consider a localised loading at the edge of a semi-infinite beam. When such a beam is supported by an elastic foundation and is under a loading P acting downwards at its edge, a vertical deflection is generated in the beam so that a bending moment M arises. The latter is analogous to the flexural strain used in WIM as it is based on the second derivative of the beam's vertical profile

$$M = -EI\frac{\mathrm{d}^2 y}{\mathrm{d}x^2}, \tag{1.6}$$

where E and I are respectively the elastic modulus and moment of inertia of the beam (Hétenyi, 1946). The mathematical expression of the bending moment caused by the forcing on the beam is

$$M = -\frac{P}{\mu}e^{-\mu x}\sin\mu x, \qquad \mu = \left(\frac{k_f}{4EI}\right)^{\frac{1}{4}} \tag{1.7}$$

where k_f is the foundation modulus, which can be viewed as a Hooke's constant, and x is the axial direction of the beam (Hétenyi, 1946). Taking the first-order derivative of Eq. (1.7) and equalling it to zero we obtain

$$e^{-\mu x}(\cos\mu x - \sin\mu x) = 0 \tag{1.8}$$

which is satisfied when $x \to \infty$ or $x = (4n+1)\pi/4\mu$ and where $n = 0, 1, 2, ...$ This implies that the position of the maximum bending moment, and therefore of maximal deformation, caused

by a point loading at the edge of a semi-infinite beam supported by an elastic foundation is

$$x^* = \frac{\pi}{4}\left(\frac{4EI}{k_f}\right). \tag{1.9}$$

With the following equivalences for the elastic modulus (Boutin et al., 2018), moment of inertia (Hétenyi, 1946) and foundation modulus (Boutin et al., 2018)

$$E = Y^*, \quad I = \frac{h^3}{12(1-\nu^2)}, \quad k_f = \rho_w g$$

where Y^* is the effective Young's modulus of sea ice and h its thickness, ν is the Poisson ratio, ρ_w is the sea water density and g is gravitational acceleration, it is possible to write a final expression for x^*

$$x^* = \frac{\pi}{4}\left(\frac{Y^* h^3}{3\rho_w g(1-\nu^2)}\right)^{1/4}. \tag{1.10}$$

Mellor (1983) was the first to consider this framework for determining a flexure-induced fracture distance in the context of ice rafting, not for the case of wave-induced breakup. He wrote that "*when the ice is flexed, it will tend to break first at a distance x^* from the free edge*". This comment has led Toyota et al. (2011) to consider that x^* is "*the minimum ice length at which breakup will occur due to flexure stress*", Williams et al. (2013a) to interpret x^* as "*[corresponding] to the diameter below which flexural failure cannot occur*" and Boutin et al. (2018) to assume x^* is the diameter "*below which [...] no flexural failure is possible*". But, since WIM use $\lambda/2$ as the maximal floe size and that this length comes from inferring that sea ice will break at the extrema of deformation, shouldn't x^* be also considered as a maximum floe length scale since it lies on the same mathematical premises ?

With that said, the GSL NFSDs and AFSD (Figs. 15 (a-c) and 16a) are compared to both one half of the measured wavelength and to x^* in order to see if these quantities could represent the maximum floe size generated in the experiments. The same was made for the NFSDs and AFSD of the NBB (Figs. 15 (b-d) and 16b) but since the wavelength could not

be measured in this experiment, a theoretical reference value was computed with Eq. (1.4) and reduced by the same factor (0.8667× lower than the incoming wavelength) than the one observed for the reduction of wavelength in the GSL. In order to obtain values for x^*, the sea ice effective Young's modulus and thickness have to be known. Using Eq. (1.3), a reference value of 10 GPa for Young's modulus (Y_0), a range of 0.05 to 0.1 (50 to 100 ppt) for brine volume (v_b) and a reduction of 0.5 GPa in order to correct for material fatigue due to low period waves having a period close to 4 s (Williams et al., 2013a), maximal and minimal effective Young's modulus values are obtained to be

$$[Y^*_{\text{min}}, Y^*_{\text{max}}] = [5.990, 7.745] \quad \text{GPa}. \tag{1.11}$$

Knowing that sea ice used in the GSL experiment had its thickness ranged between 10 and 30 cm and by having in hand reference values for the effective Young modulus, x^* could be plotted for 10 (x^*_{10}), 20 (x^*_{20}) and 30 (x^*_{30}) cm thick ice. The extent of the shaded areas is determined by the minimum and maximum values of x^* given the range of Young's modulus for a fixed thickness and the solid line is the mean value. The same thing was made for the NBB experiment but for thickness values of 40 (x^*_{40}) and 60 (x^*_{60}) cm.

It can be seen in Figure 15 and 16 that x^* is more sensitive to changes in thickness than to Young's modulus value so that in order to do a good comparison of the bending moment-based theory against observations, ice thickness needs to be well constrained. Unfortunately, this is not the case in our experiments. But, based on the fact that x^* and $\lambda/2$ should both represent the maximal floe length due to flexure and since it is the only mechanism which can have caused the largest floes in our data – thermal cracking and fracture by isostatic ajustment have not occured during the experiments – there should be no floe having sizes greater than x^* or $\lambda/2$. This statement allows to conclude that the thickness of the ice over which the images were recorded in the GSL experiment might have been close to 30 cm while for the NBB, it should have been over 60 cm. Note that in the NBB experiment, ice thickness was not measured directly in the area where images were recorded to create Figure 6. Before the

fragmentation, only the edge of the initial ice plate was available for measuring thickness and a value of 5 ± 2.5 cm was assessed. After the break up had occurred, the thickness was measured to be between 40 and 60 cm for floes of ice which were further into the pack but still relatively close to its edge since the zodiac boat could not sail up to the center of the pack. There was therefore a horizontal variation of thickness within the ice plate used for the NBB experiment. It is thus plausible that the thickness was greater in the area were images were taken (i.e. in the center of the floe) so that if it had been measured there, x^* would adequately represent the maximal size of the NBB AFSD. Moreover, the fact that AFSDs are modally distributed highlights that sea ice does not systematically break up *first* at the position where lies the maximum strain and hence that it is *possible* for sea ice to break up at strains below that threshold, a result that is coherent with the concept of material fatigue brought by Langhorne et al. (1998).

In the end, what is the most accurate representation for the maximal size caused by wave-induced sea ice breakup ? Figure 16a shows that $D_{\max}$ is better described by x^* than by $\lambda/2$ and Figure 16b shows that neither the approximated theoretical value for $\lambda/2$ nor x^* fits well with the maximum observed floe size. As mentioned above, the latter may have been caused by an erroneous measurement of ice thickness so that in reality x^* might also well describe $D_{\max}$ in this experiment. The lack of correlation of the wavelength-dependent parameterization with the maximum floe size in both experiment is thought to be a clear indication that it does not represent the break up of sea ice by ocean waves adequately. It is rather the more physically-based approach which relies on ice thickness and elasticity to assess $D_{\max}$ that has given a more convincing result. It is thus tempting to conclude that the extent of the FSD is controlled by the flexural rigidity of sea ice and is not dependent on wave properties but more experiments of this kind, where ice thickness is better constrained, are needed to test this hypothesis.

1.6.3.4 From observations to models

As mentionned in the introduction, the observational studies about the FSD mainly uses the number density (ND) but why ? Given that the propagation of waves into sea ice is a vast field of study and since this process depends on the number of floes (Roach, 2019), it might have been seen as helpful to use a ND to plot the FSD. In a wide range of studies, where a lot of different locations have been sampled at various resolutions, there is indication that the ND follows an upper-truncated power law (see Table 1 of Stern et al., 2018b). Hence, when sea ice has been influenced by multiple mechanical and thermodynamical processes, such as lateral melting, advection, freezing together of multiple floes and wave-induced breakup, the ND of floes for a given area is indeed well described by a power law.

In modelling studies made by Dumont et al. (2011), Williams et al. (2013a,b), Boutin et al. (2018), Bateson et al. (2019) and Boutin et al. (2020), the shape of the number density is directly translated into a *probability* density, the latter of which can even have its probabilities based on the surface of the floes (Boutin et al., 2020). This latter framework therefore assumes that the AFSD has the same shape as the NFSD; an incorrect assumption according to our results. Since climate models are using either a constant value for floe size or simply not considering it, these attempts of FSD inclusion help understand the impact of a variable floe size on sea ice concentration, melt, extent and so on. But, is it correct to translate directly from a number density to a probability density ? In fact, constructing the probability density function with the number density relies on the assumption that floe size is a stochastic variable, the same way we construct the probability density of a dice by it's number of faces. Since the surface of a floe is indicative of its mass and that the mass of a floe indicate its prominence relative to thermodynamical and mechanical processes, floe extent should be used to calculate the PDF rather than floe number. Another motivation towards using the AFSD is that the number density and the NFSD can be obtained from it but no information on the area of floes is contained in the NFSD. That way, an area-dependent process (e.g. lateral melt) could not be computed from the NFSD but a number-dependent process (e.g.

wave attenuation) could be computed using the AFSD. Furthermore, in the Los Alamos Sea Ice model (CICE) the ice thickness distribution (ITD) is represented as a probability density function from which the probability $g(\mathbf{x}, h, t)\ dh$ of a thickness category $(h,\ h+dh)$ is defined as "*the fractional area covered by ice in the thickness range* $(h,\ h+dh)$ *at a given time [t] and location [***x***]*" (Hunke and Lipscomb, 2010). With the fact that the representation of sea ice in large scale coupled climate models as a joint floe size and thickness distribution (FSTD) (Horvat and Tziperman, 2015; Zhang et al., 2015) is the eventual milestone in large scale sea ice modelling, the probability densities for both size and thickness should be based on the same metric in order to have a coherent approach.

In order to have a more physically-based implementation of floe size in WIMs, a PDF weighted by the respective area of floes rather than by their number should be used to represent the FSD. Moreover, our data shows that the wave-induced breakup component of the FSD could be parametrized as a modal distribution bounded by eq. (1.10) in order to be more physically-based than assuming a power-law distribution bounded by one half of the dominant wavelength. If the goal is to model large scale sea ice dynamics, the use of a power law distribution is appropriate as it results from all the processes affecting the morphology of the ice. Yet the influence of wave-induced break-up on the global FSD should not be to solely change $D_{\max}$ but also to generate preferential sizes.

Focusing more on sea ice than waves in order to establish a WIM, Zhang et al. (2015) have constructed a FSTD model by adding a formalism for the FSD to the ITD framework brought by Thorndike et al. (1975) and Hibler (1980) where break-up is parameterized with the help of a redistribution probability function $Q(d)$, where d is the floe size, and a redistributor $\beta(d_1, d_2)$, where d_1 is the initial size and d_2 is the breakup-resulting size. $Q(d)$ is based on the mathematical expression of the ridging probability (Thorndike et al., 1975; Hibler, 1980) and specifies whether the ice breaks or not and if so what sizes will be broken up. On the other hand, $\beta(d_1, d_2)$ specifies into which size categories the ice will be redistributed. As no wave module is available in the model of Zhang et al. (2015) to establish a fragmentation proba-

bility as is made in WIMS (e.g. Williams et al., 2013a), a breakup constant is parametrized with the help of wind speed, open-ocean surface, floe size and thickness as these variables are thought to influence the probability of a breakup event. For example, great wind speeds and fetch will lead to a more energetic wave field which can cause breakup to happen. Rather than using observationnal studies to impose a shape to the FSD, the power law shape of the cumulative floe number distribution leads Zhang et al. (2015) to the assumption that "*ice fragmentation caused by stochastic ocean surface is likely to be a random process such that [...] no particular size category is favored against other size categories during the breakup process*" when elaborating the shape of $\beta(d_1, d_2)$. In this framework, all resulting sizes d_2 being within a certain range lower than the intial size d_1 are thus equally probable of being generated. However, as can be seen in Figure 16, a fragmentation event does not cause a uniform distribution but rather generates a preferential size to come out of the process. A minor change in the form of $\beta(d_1, d_2)$ from a uniform redistribution to a preferential redistribution depending on d_2 could be more physically sound.

1.7 Conclusion

In order to better understand the physics of wave-induced sea ice breakup, a UAV was used to capture the fragmentation produced by ship-generated waves. Two experiments were conducted, one in the Gulf of St. Lawrence, Québec, and the other in the northern part of Baffin Bay. Three main branches of the break-up have been analyzed : the span of fracture, the transient evolution of break-up and the resulting FSDs. Regarding the extent of fracture, the fact that the ice broke more during the NBB experiment is thought to be attributable to the difference in ship speed between the experiments, to the high brine volume and to a thickness-dependent resonance (Fox and Squire, 1991). In fact, all of these factors possibly contributed to a greater span of fracture but determining the role of each is not possible here.

Using the first-order theory of Kelvin ship waves (Thomson, 1887), theoretical values for incident wave properties were calculated and were compared to what was observed in the

ice. It was obtained for the GSL that both the wavelength and phase speed have been reduced by the change in impedance of the water surface but that there is no significant difference for the wave angle of propagation and period. For the NBB experiment, data indicates that there is a gap between the angle of floes and the one at which incident waves propagate. This result is thought to be attributable to the fact that the theoretical reference angle value might not be usable in this case as the ship had a heavily curved path while accelerating toward the floe. Regarding breakup itself, its speed has been identified to be roughly 40 % of the wave phase speed so that it seems reasonable, given the adequate grid scale and time step, to assume breakup to be instantaneous.

With the help of both watershed-based image processing and manual segmentation, floe size PDFs were obtained and were used as the representation of the FSD. The minor axis has been considered as the characteristic length scale since it is the dimension generated by ice flexure. It has been shown that using the number of floes to construct the PDF leads to the misrepresentation of the preferential size, the latter being better illustrated by using the ratio between floe surface and the entire area of sea ice within the image to establish probabilities. The displacement of the modal floe size to a higher value with increasing thickness has been observed but as the ship speed, and hence the wave structure, was different in each experiment, it is not possible to conclude that the flexure-favored length scale is solely dependent on ice properties and not on waves. It has been shown that the semi-infinite beam theory (Hétenyi, 1946) might be a physically-based contender to represent the maximum allowed floe size generated by wave-induced breakup. A note has been made regarding the use of a power law-shaped ND as a PDF in coupled spectral wave-ice models (Dumont et al., 2011; Williams et al., 2013a,b; Boutin et al., 2018; Bateson et al., 2019). Finally, a more physically-based parameterization would model wave-induced break-up not as a function that changes the maximum floe size while assuming a power law distribution, but rather as a function that would generate a Gaussian distribution which has its maximum value limited by x^*. It has also been noted that the presence of a preferential size challenges the assumptions on which the redistribution theory of Zhang et al. (2015) is based.

CONCLUSION GÉNÉRALE

En générant des vagues près de grandes plaques de glace de mer à l'aide du *NGCC Amundsen*, deux évènements de fragmentation de la banquise en milieu naturel ont été simulés expérimentalement. La taille des floes résultants de ces expériences ainsi que l'évolution temporelle du processus ont été enregistrées à l'aide d'un ATP. Cela a permis de mieux comprendre comment les vagues sont affectées par la présence de glace à la surface de l'océan, de voir à quelle vitesse la fragmentation se produit et d'isoler l'influence des vagues sur la FSD.

Dans l'expérience du GSL, il a été observé que la longueur d'onde et la vitesse de phase sont réduites de 13% lorsque les vagues entrent dans la banquise, un résultat qui concorde qualitativement avec celui observé par Liu and Mollo-Christensen (1988) dans des conditions où des vagues naturelles ont fragmenté la glace. Dans l'expérience du GSL, la valeur la plus fréquente de l'histogramme d'orientation des floes est à l'intérieur de l'incertitude de l'angle de propagation des vagues alors que dans la NBB, la situation est différente. Le mode de la distribution d'orientation des floes se situe à $21.4 \pm 4^{\circ}$ de la valeur de référence calculée à l'aide de la théorie linéaire des vagues de navire (Thomson, 1887). Il est toutefois estimé que cette différence est attribuable à la trajectoire non-rectiligne du navire lors de son accélération et non pas à la physique du processus. En ce qui concerne la vitesse de fragmentation, il a été obtenu que celle-ci représentait 39.4% de la vitesse de propagation des vagues dans la glace. Dans un contexte de modélisation, la fragmentation pourrait donc être considérée comme instantanée si le pas de temps est supérieur à $\sim$1 minute et que la résolution spatiale est supérieure à $\sim$100 m.

En utilisant la fréquence d'observation des floes afin d'établir la PDF, la taille préférentielle des floes observée dans les deux expériences n'est pas bien représentée. Malgré le fait que les floes ayant une taille proche de la taille préférentielle représentent la majorité de la masse de glace dans l'image, ceux-ci sont associés a une probabilité d'occurence bien

moindre que les petits floes, car moins nombreux. Pour remédier à ce problème, une nouvelle approche à été proposée, laquelle utilise le ratio entre la surface des floes et la surface totale de glace dans l'image pour construire la PDF. Avec cette démarche, la distribution de masse de glace est bien représentée et met en valeur, par sa forme modale, la présence claire d'une taille préférentielle. Cette observation est en accord avec les conclusions obtenues par Squire (1995) et Herman (2017) que la fragmentation génère une taille préférentielle. De plus, Fox and Squire (1991), Squire (1995), Herman (2017) et Herman et al. (2018) mentionnent aussi que cette taille préférentielle devrait être contrôlée par l'épaisseur et la rigidité de la glace, tout en étant indépendante de la structure des vagues. Malheureusement, cette hypothèse n'a pu être confirmée étant donné que le navire n'avait pas la même vitesse de croisière dans les deux expériences. Cela fait en sorte que l'augmentation observée de la valeur du mode de la AFSD ne peut être directement attribuable au changement d'épaisseur de la glace entre les deux expériences.

Les AFSDs ont aussi été comparées aux distances de fracture ($\lambda/2$ et x^*) provenant de deux théories différentes de déformation de la glace. L'une est basée sur le fait que la glace se conforme instantanément et complètement à un niveau d'eau sinusoïdal sans en atténuer l'amplitude et est adoptée par différents WIMs (e.g. Dumont et al., 2011), alors que l'autre se base sur la physique de la déformation d'une poutre semi-infinie reposant sur un medium élastique et forcée à son extrémité (Hétenyi, 1946). Il a été obtenu que x^* concorde avec la taille maximale des floes dans l'expérience GSL alors que $\lambda/2$ surestime celle-ci. Dans la baie de Baffin, à la fois $\lambda/2$ et x^* sous-estiment la taille maximale. Or, le fait que l'épaisseur de la glace ait été mesurée en bordure du floe et non à l'intérieur de la zone imagée – qui se trouvait elle-même plus au centre – mène à l'hypothèse que l'épaisseur de la glace considérée pour analyse aurait pu être supérieure à la valeur mesurée, ce qui aurait potentiellement résulté en une meilleure corrélation entre x^* et la taille maximale. L'étendue de la AFSD semble donc mieux décrite par la théorie de Hétenyi (1946) que par celle de Dumont et al. (2011), ce qui porte à croire que la taille des floes résultants de la fragmentation est contrôlée par l'épaisseur et la rigidité de la glace et qu'elle est indépendante de la longueur d'onde des vagues. Or, il

s'agit là d'une seule observation. Il serait donc nécessaire de réaliser d'autres expériences du même type où l'épaisseur et la rigidité de la glace seraient mesurées avec une plus grande précision et que les caractéristiques des vagues soient elles aussi mesurées.

Une perspective intéressante de ce projet serait la création d'un outil qui, en inversant l'équation (1.10) et en utilisant la taille maximale de la AFSD comme valeur de référence pour x^*, permettrait d'identifier l'épaisseur de la glace à partir d'images de glace fragmentée. Il faudrait bien sûr faire plus d'expériences pour vérifier si la théorie derrière x^* représente bien la taille maximale des floes avant de la considérer comme référence. Si une telle vérification s'avérait concluante, l'installation de caméras sur les brises glaces de la flotte de la garde côtière canadienne pourrait permettre de fournir des données in situ au service canadien des glaces pour la construction des cartes de glace. Afin de rendre opérationnel un tel outil, un algorithme de segmentation automatisé et fiable devrait être développé conjointement avec un algorithme qui servirait à identifier les types de glace (nilas, grise, blanche, etc.). Dans une optique de calibration de la rigidité de la glace, des campagnes de terrains pourraient être organisées dans le but de caractériser les propriétés de la glace afin d'attribuer un module de Young fidèle à la réalité en fonction du type de glace.

Voici donc comment, suite à ces avancements, l'épaisseur de la glace pourrait être identifiée. D'abord, l'algorithme identifiant le type de glace de mer est lancé pour la caractériser en fonction de ses caractéristiques visuelles. Les caméras enregistrent des images de la glace fragmentée par les vagues en périphérie du navire jusqu'à ce qu'un changement notable du type de glace soit perçu par l'algorithme. Ensuite, l'algorithme automatisé de segmentation crée la AFSD pour la glace du premier type identifié. L'épaisseur de cette glace est ensuite calculée en prenant la taille maximale de la AFSD et en insérant le Y^* correspondant au type de glace enregistré dans l'équation (1.10) inversée. Les même étapes seraient suivies lors du deuxième changement de type, ce qui résulterait en une carte géoréférencée de l'épaisseur et du type de glace.

ANNEXE I

A NOTE ON SHIP WAVES

Cette annexe a été écrite en anglais car elle sera présente dans l'article "*Aerial observations of sea ice break up by ship induced waves*".

Waves generated by a moving ship follow a symmetrical V-shaped pattern called the Kelvin wake. Under the assumptions of an irrotational and inviscid fluid, a quite simple mathematical description of these waves can be made using a velocity potential ϕ and the linear Airy wave theory. By applying the linear free-surface conditions and by not allowing normal flow at the bottom,

$$\left.\frac{\partial^2\phi}{\partial t^2}\right|_{z=0} + g\left.\frac{\partial\phi}{\partial z}\right|_{z=0} = 0\,, \qquad \eta = \frac{-1}{g}\left.\frac{\partial\phi}{\partial t}\right|_{z=0}, \qquad \left.\frac{\partial\phi}{\partial z}\right|_{z=H} = 0 \tag{2.1}$$

where g is the gravitational acceleration, a solution for the velocity potential can be obtained. By substituting a general *ansatz*

$$\phi(x,z,t) = A\mathcal{R}e\Big\{\varphi(x,z)e^{-i\omega t}\Big\}, \qquad \varphi(x,z) = \psi(z)e^{ikx} \tag{2.2}$$

where A is the amplitude of the oscillation, ω the angular frequency and k the wavenumber, in the conditions of (2.1), one ends up with the solution

$$\phi(x,z,t) = A\mathcal{R}e\left\{\frac{ig}{\omega}\frac{\cosh k(z+H)}{\cosh kH}e^{i(kx-\omega t)}\right\}, \quad \text{only if} \quad \omega^2 = gk\tanh(kH). \tag{2.3}$$

When ocean depth is larger than half the wavelength, one can assume that $H \to \infty$ so that $\tanh kH \to 1$. Thus the deep-water dispersion relation $\omega^2 = gk$ is obtained and the velocity potential becomes

$$\phi(x, z, t) = A\mathcal{R}e\left\{\frac{ig}{\omega}e^{kz}e^{i(kx+ky-\omega t)}\right\} \tag{2.4}$$

with the z-axis pointing upward.

To obtain the solution in a frame of reference attached to a ship sailing at a steady speed U in the x direction, a change of coordinate can be made such that

$$x \to x - Ut \tag{2.5}$$

$$y \to y \tag{2.6}$$

$$z \to z \tag{2.7}$$

so that the velocity potential becomes

$$\phi(x, z, t) = A\mathcal{R}e\left\{\frac{ig}{\omega}e^{kz}e^{ik(x+y)}e^{it(kU-\omega)}\right\}. \tag{2.8}$$

As waves generated by the ship propagate in multiple directions, a rotation of the x-y plane can be made in order to obtain the solution in the inertial frame of the waves,

$$\phi(x, z, t) = A\mathcal{R}e\left\{\frac{ig}{\omega}e^{kz}e^{i(kx\cos\vartheta+ky\sin\vartheta)}e^{i(kU\cos\vartheta-\omega)t}\right\}. \tag{2.9}$$

Assuming no temporal variation of the velocity potential, the following relations can be obtained

$$kU\cos\vartheta = \omega \quad \Rightarrow \quad c_p = \frac{\omega}{k} = U\cos\vartheta. \tag{2.10}$$

Combining this phase speed to the deep-water wave dispersion relation gives the following relation for the wavelength generated by the ship

$$\lambda(U, \vartheta) = \frac{2\pi U^2}{g} \cos^2 \vartheta. \tag{2.11}$$

Inserting Eq. (2.11) into (2.10) gives the wave period as a function of ship speed and wave direction,

$$T(U, \vartheta) = \frac{2\pi U}{g} \cos \vartheta. \tag{2.12}$$

A derivation of the wave group velocity using (2.10) leads to the conclusion that V-shaped pattern of waves generated by a ship has, in the first order approximation, an aperture of 38.934° (Sorensen, 1973). The maximum amplitude wave generated by a moving ship propagates at an angle of $\theta_{\text{wave}} = \sin^{-1}\left(1/\sqrt{3}\right) \simeq 35.2644°$ (Soomere, 2007). These waves stand at fixed points on the v-shaped pattern that are where constructive interference of transverse and divergent waves happen (Sorensen, 1973; Soomere, 2007). The former type of wave propagates at angles from 0° to θ_{wave} and the latter propagates at angles from 90° to θ_{wave}. Since these waves are the most prominent of those generated by the ship, θ_{wave} is used here as a reference to obtain properties of waves incident to the ice.

The derivation presented above is based on the assumption that the velocity potential is stationary, i.e. $\phi_t = 0$. This corresponds to cases where no ambient waves are present, which was the case for both experiments, or where the ship is sailing at a constant speed. Fig. 3 and Fig. 5 show the ship track and the temporal evolution of its speed for both experiments. The steady-state approximation seems more realistic for the NBB experiment than the GSL one as the time frame where the speed was stable was larger for the first than for the second. Despite that, Eq. (2.10) and (2.11) are considered as good first-order approximations for the computation of the physical properties of waves incident on sea ice.

Break-up events in the MIZ happen due to wind waves, not from ship-generated waves.

So, is breaking sea ice with waves from a ship representative of what happens in nature ? That question simplifies itself as : are wind generated waves different from ship-generated waves ? From a mathematical point of view, they both obey to the same physics as they are governed by the same dispersion relation and as their restoring force is both gravity. Their main differences are their external forcing, which influences the directional spectrum of waves. Ship waves are more constrained than wind waves as their phase speed is dictated by (2.10), and their height profile, with ship waves smoother than wind waves. This being said, it seems reasonable to claim that conclusions made from our experiments also apply to wind-generated waves.

ANNEXE II

AU-DELÀ DE L'ÉTENDUE DE GLACE ANALYSÉE DANS L'EXPÉRIENCE NBB

Dans l'article "*Aerial observations of sea ice break up by ship induced waves*" présenté dans ce mémoire, il a été choisi de ne présenter qu'une partie de la surface de glace imagée lors de l'expérience NBB (Figure 6). Dans cette zone de l'orthomosaïque, la taille et l'angle des floes résultants de la fragmentation suivent une dimension et une orientation préférentielles. Deux raisons principales nous ont menées à considérer uniquement la Figure 6 pour analyse : 1) la tendance morphologique représente la majorité de la surface imagée et 2) la segmentation manuelle a été obligatoire avec ces images. Obtenir un portrait partiel mais tout de même représentatif de la globalité de la fragmentation résultante dans un délai raisonnable a semblé être un bon compromis. Au final, une segmentation complète de la Figure 17 aurait résulté en une diffusion plus importante du mode de la PDF étant donnée la plus grande variabilité morphologique des floes non considérés pour l'analyse. Autrement dit, l'écart-type de la AFSD aurait été plus grand, mais les conclusions auraient été les mêmes.

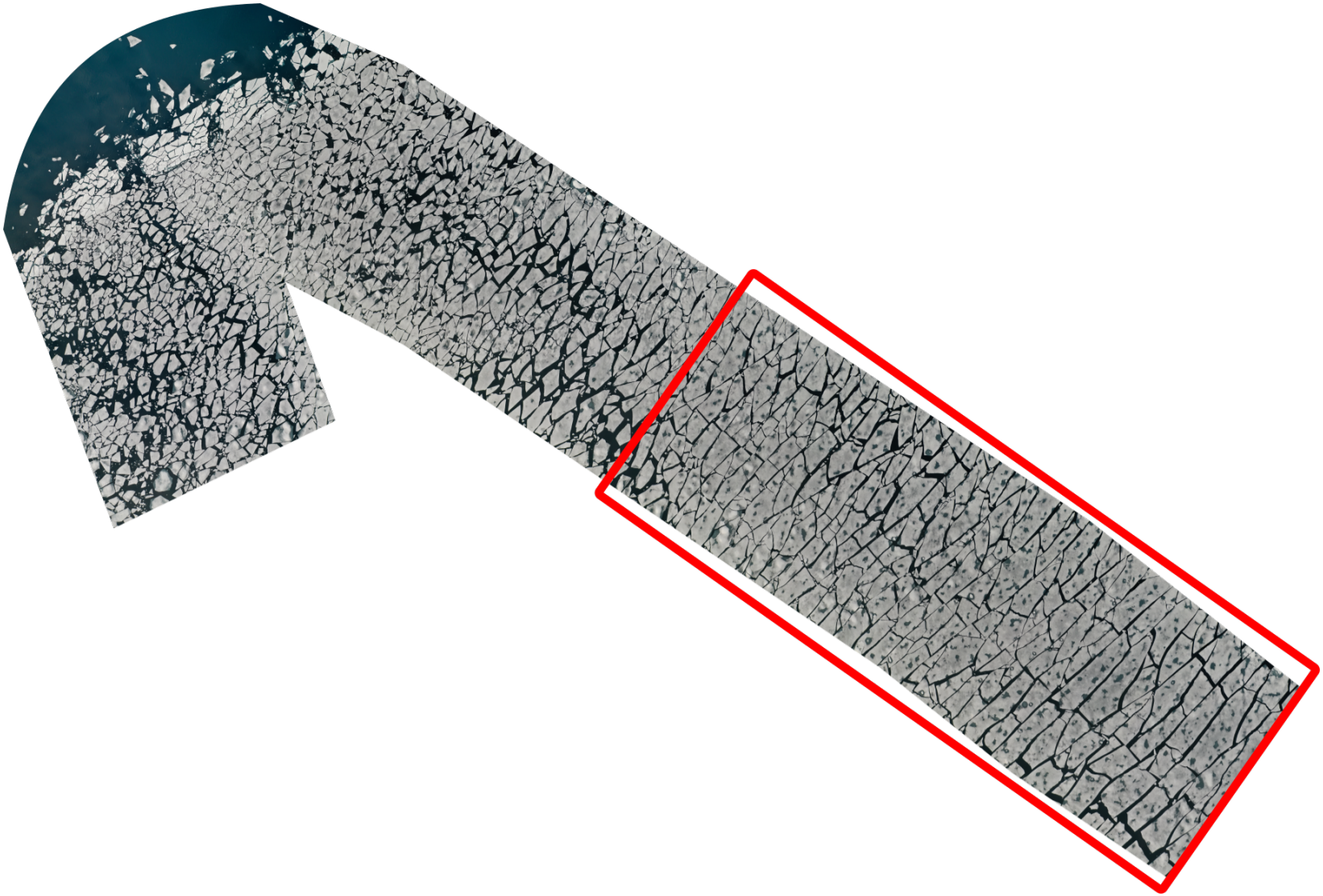

Figure 17: Orthomosaïque complète de la fracture résultante dans l'expérience NBB. La section considérée pour analyse est indiquée par le rectangle rouge.

RÉFÉRENCES

Alberello, A., Onorato, M., Bennetts, L., Vichi, M., Eayrs, C., Machutchon, K., Toffoli, A., 2019. Brief communication: Pancake ice floe size distribution during the winter expansion of the Antarctic marginal ice zone. Cryosphere 13 (1), 41–48.

Arrigo, K. R., 2016. Sea ice as a habitat for primary producers. In: Sea Ice: Third Edition.

Asplin, M. G., Galley, R., Barber, D. G., Prinsenberg, S., 2012. Fracture of summer perennial sea ice by ocean swell as a result of Arctic storms. Journal of Geophysical Research: Oceans 117 (C6).

Barrette, C., Brown, R., Way, R., Mailhot, A., Diaconescu, E., Grenier, P., Chaumont, D., Dumont, D., Sévigny, C., Howell, S., Senneville, S., 2020. Chapter 2: Nunavik and Nunatsiavut regional climate information update. ArcticNet Inc., Québec, Canada.

Bateson, A. W., Feltham, D. L., Schröder, D., Hosekova, L., Ridley, J. K., Aksenov, Y., 2019. Impact of floe size distribution on seasonal fragmentation and melt of Arctic sea ice. The Cryosphere Discussions.

Bennetts, L. G., O'Farrell, S., Uotila, P., 2017. Brief communication: Impacts of ocean-wave-induced breakup of Antarctic sea ice via thermodynamics in a stand-alone version of the CICE sea-ice model. Cryosphere.

Bennetts, L. G., Peter, M. A., Squire, V. A., Meylan, M. H., 2010. A three-dimensional model of wave attenuation in the marginal ice zone. Journal of Geophysical Research: Oceans 115 (12).

Boutin, G., Ardhuin, F., Dumont, D., Sévigny, C., Girard-Ardhuin, F., Accensi, M., 2018. Floe Size Effect on Wave-Ice Interactions: Possible Effects, Implementation in Wave Model, and Evaluation. Journal of Geophysical Research: Oceans 123 (7), 4779–4805.

Boutin, G., Lique, C., Ardhuin, F., Talandier, C., Accensi, M., Girard-Ardhuin, F., Rousset, C., 2020. Towards a coupled model to investigate wave-sea ice interactions in the Arctic marginal ice zone. Cryosphere 14 (2).

Casas-Prat, M., Wang, X. L., 2020. Projections of Extreme Ocean Waves in the Arctic and Potential Implications for Coastal Inundation and Erosion. Journal of Geophysical Research: Oceans.

Cavalieri, D. J., Parkinson, C. L., 2012. Arctic sea ice variability and trends, 1979-2010. The Cryosphere 6 (4), 881.

Comiso, J. C., Parkinson, C. L., Gersten, R., Stock, L., 2008. Accelerated decline in the Arctic sea ice cover. Geophysical Research Letters.

Cunsolo Willox, A., Harper, S. L., Ford, J. D., Landman, K., Houle, K., Edge, V. L., 2012. "From this place and of this place:" Climate change, sense of place, and health in Nunatsiavut, Canada. Social Science and Medicine 75 (3).

Dawson, J., Pizzolato, L., Howell, S. E., Copland, L., Johnston, M. E., 2018. Temporal and spatial patterns of ship traffic in the Canadian arctic from 1990 to 2015. Arctic 71 (1).

Dumont, D., Kohout, A., Bertino, L., 2011. A wave-based model for the marginal ice zone including a floe breaking parameterization. Journal of Geophysical Research: Oceans 116 (C4).

Fox, C., Squire, V. A., 1991. Strain in shore fast ice due to incoming ocean waves and swell. Journal of Geophysical Research.

Guimarães, P. V., Ardhuin, F., Sutherland, P., Accensi, M., Hamon, M., Pérignon, Y., Thomson, J., Benetazzo, A., Ferrant, P., 2018. A surface kinematics buoy (SKIB) for wave-current interaction studies. Ocean Science 14 (6).

Herman, A., 2010. Sea-ice floe-size distribution in the context of spontaneous scaling emergence in stochastic systems. Physical Review E 81 (6), 66123.

Herman, A., 2017. Wave-induced stress and breaking of sea ice in a coupled hydrodynamic discrete-element wave-ice model. Cryosphere.

Herman, A., Evers, K. U., Reimer, N., 2018. Floe-size distributions in laboratory ice broken by waves. Cryosphere 12 (2), 685–699.

Hétenyi, M., 1946. Beams On Elastic Foundation Theory With Applications In The Fields Of Civil And Mechanical Engineering. The University Of Michigan Press.

Hibler, W. D., 1980. Modeling a variable thickness sea ice cover. Monthly Weather Review 108 (12).

Holt, B., Martin, S., 2001. The effect of a storm on the 1992 summer sea ice cover of the Beaufort, Chukchi, and East Siberian Seas. Journal of Geophysical Research: Oceans 106 (C1), 1017–1032.

Horvat, C., Tziperman, E., 2015. A prognostic model of the sea-ice floe size and thickness distribution. The Cryosphere 9 (6), 2119–2134.

Hunke, E. C., Lipscomb, W. H., 2010. CICE : the Los Alamos Sea Ice Model Documentation and Software User ' s Manual LA-CC-06-012. Research Report, 1–76.

Huntington, H. P., Gearheard, S., Holm, L. K., Noongwook, G., Opie, M., Sanguya, J., 2016. Sea ice is our beautiful garden: Indigenous perspectives on sea ice in the Arctic. In: Sea Ice: Third Edition.

Hwang, B., Ren, J., McCormack, S., Berry, C., Ayed, I. B., Graber, H. C., Aptoula, E., 2017. A practical algorithm for the retrieval of floe size distribution of Arctic sea ice from high-resolution satellite Synthetic Aperture Radar imagery. Elementa 5.

Kintisch, E., 1 2017. People of the Sea Ice See Cracks Forming. Hakai Magazine : Coastal Science and Societies.

Kohout, A. L., Meylan, M. H., 2008. An elastic plate model for wave attenuation and ice floe breaking in the marginal ice zone. Journal of Geophysical Research: Oceans 113 (9).

Kohout, A. L., Williams, M. J., Dean, S. M., Meylan, M. H., 2014. Storm-induced sea-ice breakup and the implications for ice extent. Nature.

Krupnik, I., Jolly, D., 2002. The Earth Is Faster Now: Indigenous Observations of Arctic Environmental Change. Frontiers in Polar Social Science.

Kwok, R., Rothrock, D. A., 2009. Decline in Arctic sea ice thickness from submarine and ICESat records: 1958–2008. Geophysical Research Letters 36 (15).

Laidre, K. L., Regehr, E. V., 2016. Arctic marine mammals and sea ice. In: Sea Ice: Third Edition.

Langhorne, P. J., Squire, V. A., Fox, C., Haskell, T. G., 1998. Break-up of sea ice by ocean waves. Annals of Glaciology.

Lasserre, F., Pelletier, S., 2011. Polar super seaways? Maritime transport in the Arctic: An analysis of shipowners' intentions. Journal of Transport Geography 19 (6).

Li, J., Ma, Y., Liu, Q., Zhang, W., Guan, C., 2019. Growth of wave height with retreating ice cover in the Arctic. Cold Regions Science and Technology 164.

Liu, A. K., Mollo-Christensen, E., 1988. Wave Propagation in a Solid Ice Pack. Journal of Physical Oceanography 18 (11).

Lu, P., Li, Z. J., Zhang, Z. H., Dong, X. L., 2008. Aerial observations of floe size distribution in the marginal ice zone of summer Prydz Bay. Journal of Geophysical Research: Oceans 113 (C2).

Markus, T., Stroeve, J. C., Miller, J., 12 2009. Recent changes in Arctic sea ice melt onset, freezeup, and melt season length. Journal of Geophysical Research 114 (C12024).
URL http://doi.wiley.com/10.1029/2009JC005436

Masson, D., Leblond, P. H., 1989. Spectral evolution of wind-generated surface gravity waves in a dispersed ice field. Journal of Fluid Mechanics 202 (12).

Mellor, M., 1983. Mechanical behavior of sea ice. Cold regions research and engineering.

Meyer, F., 1994. Topographic distance and watershed lines. Signal Processing 38 (1), 113–125.

Overland, J. E., Hanna, E., Hanssen-Bauer, I., Kim, S. J., Walsh, J. E., Wang, M., Bhatt, U. S., Thoman, R. L., Ballinger, T. J., 2019. Surface Air Temperature. Arctic Report.

Rinke, A., Maturilli, M., Graham, R. M., Matthes, H., Handorf, D., Cohen, L., Hudson, S. R., Moore, J. C., 2017. Extreme cyclone events in the Arctic: Wintertime variability and trends. Environmental Research Letters.

Roach, L., 2019. Advances in Understanding the Sea Ice Floe Size Distribution. Ph.D. thesis, Victoria University of Wellington.

Roach, L. A., Horvat, C., Dean, S. M., Bitz, C. M., 2018. An Emergent Sea Ice Floe Size Distribution in a Global Coupled Ocean-Sea Ice Model. Journal of Geophysical Research: Oceans.

Rothrock, D. A., Thorndike, A. S., 1984. Measuring the Sea Ice Floe Size Distribution. Journal of Geophysical Research 89 (C4), 6477–6486.

Smith, M., Thomson, J., 2016. Scaling observations of surface waves in the Beaufort Sea. Elementa 2016.

Soomere, T., 2007. Nonlinear components of ship wake waves. Applied Mechanics Reviews.

Sorensen, R. M., 1973. Ship-Generated Waves. Advances in Hydroscience, Academic Press inc.

Squire, V., 1995. Of Ocean Waves and Sea Ice. Annual Review of Fluid Mechanics.

Squire, V. A., 2018. A fresh look at how ocean waves and sea ice interact. Philosophical Transactions of the Royal Society A: Mathematical, Physical and Engineering Sciences 376 (2129), 20170342.

Squire, V. A., 2020. Ocean Wave Interactions with Sea Ice: A Reappraisal. Annual Review of Fluid Mechanics 52 (1).

Steele, M., 1992. Sea ice melting and floe geometry in a simple ice-ocean model. Journal of Geophysical Research: Oceans 97 (C11), 17729–17738.

Stern, H. L., Schweiger, A. J., Stark, M., Zhang, J., Steele, M., Hwang, B., 2018a. Seasonal evolution of the sea-ice floe size distribution in the Beaufort and Chukchi seas. Elementa 6.

Stern, H. L., Schweiger, A. J., Zhang, J., Steele, M., 2018b. On reconciling disparate studies of the sea-ice floe size distribution. Elementa.

Stopa, J. E., Ardhuin, F., Girard-Ardhuin, F., 2016. Wave climate in the Arctic 1992-2014: Seasonality and trends. Cryosphere 10 (4).

Thomson, J., Rogers, W. E., 2014. Swell and sea in the emerging Arctic Ocean. Geophysical Research Letters 41 (9), 3136–3140.

Thomson, W., 1887. On Ship Waves. Trans. Inst. Mech. Eng. 8, 409–433.

Thorndike, A. S., Rothrock, D. A., Maykut, G. A., Colony, R., 1975. The thickness distribution of sea ice. Journal of Geophysical Research 80 (33), 4501–4513.

Timco, G. W., Weeks, W. F., 2010. A review of the engineering properties of sea ice. Cold Regions Science and Technology 60 (2), 107–129.
URL http://dx.doi.org/10.1016/j.coldregions.2009.10.003

Toyota, T., Enomoto, H., 2002. Analysis of sea ice floes in the Sea of Okhotsk using ADEOS/AVNIR images. In: Proceedings of the 16th IAHR International Symposium on Ice, Dunedin, New Zealand. pp. 211–217.

Toyota, T., Haas, C., Tamura, T., 2011. Size distribution and shape properties of relatively small sea-ice floes in the Antarctic marginal ice zone in late winter. Deep Sea Research Part II: Topical Studies in Oceanography 58 (9-10), 1182–1193.

Toyota, T., Takatsuji, S., Nakayama, M., 2006. Characteristics of sea ice floe size distribution in the seasonal ice zone. Geophysical research letters 33 (2).

Weeks, W. F., Tucker III, W. B., Frank, M., Fungcharoen, S., 1980. Characterization of surface roughness and floe geometry of Sea Ice over the Continental Shelves of the Beaufort and Chukchi Seas. In: Symposium on Sea Ice Processes and Models. Vol. 2. pp. 32–41.

Williams, T. D., Bennetts, L. G., Squire, V. A., Dumont, D., Bertino, L., 2013a. Wave–ice interactions in the marginal ice zone. Part 1: Theoretical foundations. Ocean Modelling 71, 81–91.

Williams, T. D., Bennetts, L. G., Squire, V. A., Dumont, D., Bertino, L., 2013b. Wave–ice interactions in the marginal ice zone. Part 2: Numerical implementation and sensitivity studies along 1D transects of the ocean surface. Ocean Modelling 71, 92–101.

Zhang, J., Schweiger, A., Steele, M., Stern, H., 2015. Sea ice floe size distribution in the marginal ice zone: Theory and numerical experiments. Journal of Geophysical Research: Oceans 120 (5).

Zhang, J., Stern, H., Hwang, B., Schweiger, A., Steele, M., Stark, M., Graber, H. C., 2016. Modeling the seasonal evolution of the Arctic sea ice floe size distribution. Elementa.

Zhang, Q., Skjetne, R., 2014. Image techniques for identifying sea-ice parameters. Modeling, Identification and Control 35 (4), 293–301.

Zhang, Q., Skjetne, R., 2015. Image processing for identification of sea-ice floes and the floe size distributions. IEEE Transactions on Geoscience and Remote Sensing 53 (5), 2913–2924.

Zhang, Q., Skjetne, R., 2018. Sea Ice Image Processing with MATLAB. Taylor & Francis.

Zhang, Q., Skjetne, R., Løset, S., Marchenko, A., 2012. Digital image processing for sea ice observations in support to arctic DP operations. In: Omae. Rio de Janeiro.

Zhang, Q., Skjetne, R., Su, B., 2013. Automatic image segmentation for boundary detection of apparently connected sea-ice floes. In: Proceedings of the International Conference on Port and Ocean Engineering under Arctic Conditions, POAC. No. 2012.